

Symmetry-breaking bifurcations in two-dimensional square vortex flows

Cite as: Phys. Fluids **33**, 094112 (2021); <https://doi.org/10.1063/5.0061658>

Submitted: 28 June 2021 . Accepted: 16 August 2021 . Published Online: 21 September 2021

 Balachandra Suri



View Online



Export Citation



CrossMark

Physics of Fluids

SPECIAL TOPIC: Flow and Acoustics of Unmanned Vehicles

Submit Today!



Symmetry-breaking bifurcations in two-dimensional square vortex flows

Cite as: Phys. Fluids **33**, 094112 (2021); doi: 10.1063/5.0061658

Submitted: 28 June 2021 · Accepted: 16 August 2021 ·

Published Online: 21 September 2021



View Online



Export Citation



CrossMark

Balachandra Suri^{1,2,a)} 

AFFILIATIONS

¹School of Physics, Georgia Institute of Technology, Atlanta, Georgia 30332, USA

²Department of Mechanical Engineering, Indian Institute of Science, Bengaluru, India

^{a)}Author to whom correspondence should be addressed: balachandra@iisc.ac.in

ABSTRACT

We present a theoretical study of spatial symmetries and bifurcations in a laterally bounded two-dimensional flow composed of approximately square vortices. The numerical setting simulates a laboratory experiment wherein a shallow electrolyte layer is driven by a plane-parallel force that is nearly sinusoidal in both extended directions. Choosing an integer or half-integer number of forcing wavelengths along each direction, we generate square vortex flows invariant under different spatial symmetries. We then map out the sequence of symmetry-breaking bifurcations leading to the formation of fully asymmetric flows. Our analysis reveals a gallery of pitchfork and Hopf bifurcations, both supercritical and subcritical in nature, resulting in either steady or time-dependent asymmetric flows. Furthermore, we demonstrate that different types of flows (steady, periodic, pre-periodic, or quasi-periodic), at times with twofold multiplicity, emerge as a result of symmetry-breaking bifurcations. Our results also provide new theoretical insights into previous experimental observations in quasi-two-dimensional square vortex flows.

Published under an exclusive license by AIP Publishing. <https://doi.org/10.1063/5.0061658>

I. INTRODUCTION

Weakly driven fluid flows are often spatially symmetric due to equivariance of their governing equations, geometry of physical boundaries, and/or spatial modulation of body forces. For instance, laminar flow in a straight pipe with a circular (or square) cross section is invariant under continuous (discrete fourfold) azimuthal rotations. When driven strongly, however, real-world flows always become spatially asymmetric and, eventually, spatiotemporally chaotic. Interestingly, the onset of spatial asymmetry can be either gradual (supercritical) or sudden (subcritical), depending on whether and how a symmetric flow becomes unstable to infinitesimal asymmetric perturbations. In this article, we numerically explore symmetry-breaking bifurcations^{1–3} in a canonical two-dimensional (2D) flow composed of *approximately* (or nearly) square counter-rotating vortices. In recent years, such flows have emerged as preferred testbeds to explore diverse phenomena, such as hydrodynamic stability,^{4–9} transition to chaos,^{10,11} energy cascades and large scale flow circulations,^{11–15} chaotic mixing,¹⁶ front propagation,^{17,18} and flow control.¹⁹

Theoretically, a 2D square vortex flow is generated by driving an incompressible fluid with a force \mathbf{f} , which is sinusoidal in both spatial directions (x and y), for example, $\mathbf{f} = \sin(\pi x) \cos(\pi y) \hat{\mathbf{x}}$. Since a strictly 2D flow cannot be realized in practice, laboratory experiments

generate a quasi-two-dimensional (Q2D) flow by passing a direct current through a shallow electrolyte layer, as shown in Fig. 1. When a chessboard-like arrangement of permanent magnets is placed beneath the fluid layer, interaction between the vertical ($\pm \hat{\mathbf{z}}$) magnetic field and the electric current ($J\hat{\mathbf{y}}$) generates a horizontal Lorentz force (along $\pm \hat{\mathbf{x}}$) that drives a nearly 2D flow. Weakly driven flows in both theory and experiment are composed of a chessboard-like lattice of approximately square counter-rotating vortices. As the driving strength increases, these flows become spatiotemporally complex in a sequence of symmetry-breaking bifurcations.^{8,11–13}

Early studies have characterized the spatial features and bifurcations in square (or rectangular) vortex flows primarily using laboratory experiments.^{11,12,20,21} For instance, exploring the transition to turbulence in liquid metal layers, Sommeria¹² identified that a 2×2 lattice of square vortices loses stability via the gradual coalescing of two diagonally opposite vortices. Two distinct steady secondary states, each resulting from the merger of vortices along a different diagonal, were observed above a critical Reynolds number (Re) in separate experimental runs. Here, Re quantifies the strength of electromagnetic driving. In the same study, however, it was reported that a 6×6 lattice of square vortices undergoes sudden transition to chaos upon increasing Re only slightly above a critical value. Hence, the primary instability in

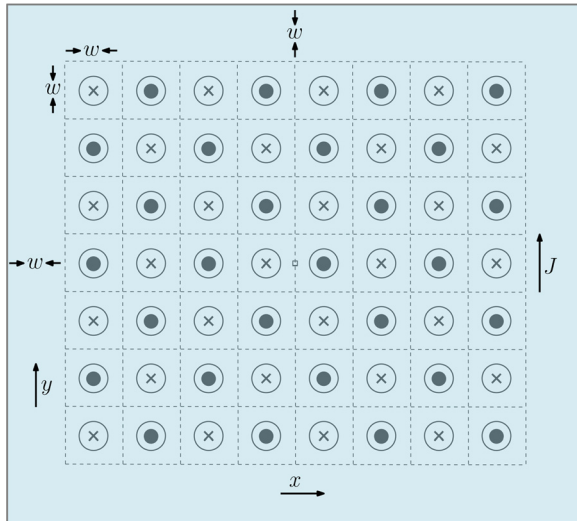


FIG. 1. Schematic of a laterally bounded, electromagnetically driven shallow fluid layer (light blue). A chessboard-like arrangement of square magnets, each of width w , placed beneath the layer creates a spatially periodic magnetic field perpendicular ($\pm \hat{z}$) to the fluid layer. A lattice of quasi-two-dimensional vortices is generated when a direct current $J\hat{y}$ passes through the electrolyte. The origin of the coordinate system is located at the center of the domain (small square). Crosses and dots represent magnetic polarization along $\pm \hat{z}$, respectively.

square vortex flows can be either supercritical or subcritical depending on the lateral extent of flow.

Unlike the square vortex flow, a 2×2 lattice of rectangular vortices in a shallow electrolyte layer [driven by $\mathbf{f} \approx \sin(\pi x/2) \cos(\pi y)\hat{\mathbf{x}}$] was found to transition directly to a time-periodic state.^{20,21} Also, such a flow was found to be dynamically sensitive to reversing the direction of forcing. Whether this sensitivity is displayed by other Q2D flows, including the square vortex flow, is currently not known. One should note that qualitatively different dynamics of the square and rectangular vortices in Refs. 12 and 21, respectively, cannot be attributed solely to their shapes, since frictional dissipation in liquid metals and electrolytes has different physical origins and magnitudes. Whether square vortex flows of comparable spatial extent and similar frictional drag undergo different types of primary instabilities was not rigorously tested in these experimental studies.

Several previous theoretical studies^{4,5,8,9,22–24} have also analyzed supercritical primary bifurcations of both square and rectangular vortex flows. For analytical and numerical convenience, however, these studies assumed that the flow satisfies free-slip or periodic velocity boundary conditions and/or is driven by a strictly sinusoidal forcing. Quantitative differences between weakly driven Q2D laboratory flows and their numerical counterparts with such idealized boundary conditions were previously reported in Refs. 4, 10, 21, and 25. In addition, Danilov *et al.*²¹ observed that a lattice of rectangular vortices in experiments undergoes gradual deformation as Reynolds number increases. The authors found that this behavior could be reproduced in a 2D direct numerical simulation (DNS) of flow only when a realistic forcing profile \mathbf{f} , reconstructed from experimental measurements, was employed. These numerical studies,^{4,21} however, did not focus on bifurcations and secondary solutions in realistic square/rectangular

vortex flows. Also, a subcritical primary instability, similar to one observed by Sommeria,¹² was not numerically identified or explored to date.

Previous experimental and numerical studies of square vortex flows also did not extensively probe how *fully* asymmetric flows emerge via symmetry-breaking bifurcations. For instance, weakly driven Q2D flows studied in Refs. 11, 12, and 21 are each invariant under a pair of twofold symmetries (e.g., reflections in x, y axes). As we shall see, primary bifurcations in such flows may not break all spatial symmetries simultaneously. Hence, the resulting secondary solutions should be continued in the Reynolds number to identify secondary, tertiary, or even quaternary bifurcations that ultimately lead to fully asymmetric flows. Michel *et al.*¹¹ have identified such a sequence of bifurcations in a 2×4 lattice of square vortices. However, symmetries of various solutions were not explicitly discussed therein.

In this article, we answer some of these questions through a systematic numerical exploration of a 2D flow composed of a chessboard-like lattice of approximately square vortices. The flow satisfies no-slip velocity boundary conditions and is driven by a forcing that closely mimics one in experiments (cf. Fig. 1). By modifying the forcing profile, we generate square vortex flows with different spatial symmetries and analyze their behavior with increasing Reynolds number. We then identify different symmetry-breaking primary bifurcations in the flow, compute the secondary solutions that consequently emerge, and thoroughly characterize their symmetries. Finally, we continue these secondary solutions in the Reynolds number and identify the sequence of (secondary, tertiary, quaternary) bifurcations that leads to the formation of fully asymmetric flows.

The article is structured as follows. In Sec. II, we discuss DNS of flow governed by a 2D model for Q2D flows in shallow electrolyte layers. In Sec. III, we identify symmetries of the governing equation for different forcing profiles. In Sec. IV, we discuss spatial features of the square vortex flow and analyze its deformation with increasing driving. Section V is a detailed exposition of symmetry-breaking primary bifurcations, with special focus on secondary states that branch out of the square vortex flow. In Sec. VI, we identify the sequence of secondary (and subsequent) bifurcations en route to the formation of fully asymmetric flows. Finally, we summarize the key findings of this study in Sec. VII and discuss their significance in the broader numerical and experimental contexts. The Newton method to compute unstable solutions, a branch continuation algorithm, and a special class of time-periodic flows are discussed in the Appendixes.

II. DIRECT NUMERICAL SIMULATION

The evolution of Q2D laboratory flows in shallow electrolyte layers is theoretically modeled using the following 2D equation:²⁶

$$\frac{\partial \mathbf{u}}{\partial t} + \beta \mathbf{u} \cdot \nabla \mathbf{u} = -\nabla p + \frac{1}{Re} (\nabla^2 \mathbf{u} - \gamma \mathbf{u}) + \mathbf{f}, \quad (1)$$

which is derived by averaging the 3D Navier–Stokes equation in the vertical (z) direction. In Eq. (1), $\mathbf{u} = u(x, y, t)\hat{\mathbf{x}} + v(x, y, t)\hat{\mathbf{y}}$ represents the horizontal velocity field at the electrolyte–air interface in experiments, p is analogous to 2D kinematic pressure, and $\mathbf{f}(x, y)$ represents the normalized, depth-averaged electromagnetic forcing. In addition, the velocity field \mathbf{u} is assumed to be divergence free ($\nabla \cdot \mathbf{u} = 0$) for weakly driven flows.^{6,26} As mentioned previously, the Reynolds number Re is related to the strength of the electromagnetic

forcing. Prefactor $\beta \neq 1$ to the nonlinear term and the linear friction term $-\gamma \mathbf{u}$ ($\gamma \neq 0$) model finite-thickness affects observed in laboratory flows. Several previous theoretical studies analyzed square vortex flows governed by Eq. (1) with $\beta = 1$. While the critical Reynolds number for each bifurcation reported in this study scales with β , the bifurcation sequence itself remains invariant for all values of $\beta > 0$. This can be easily verified by transforming the variables in Eq. (1) as follows: $\mathbf{u} \rightarrow \mathbf{u}/\sqrt{\beta}$, $\sqrt{\beta}t \rightarrow t$, and $\sqrt{\beta}Re \rightarrow Re$.

DNS of flow governed by Eq. (1) and satisfying no-slip velocity boundary conditions was performed on four different computational domains with dimensions $N_x \times N_y$, where $9 \leq N_x, N_y \leq 10$. Velocity and pressure fields on each domain were discretized on a staggered grid with spacing $\Delta x = \Delta y = 1/40$, and spatial derivatives were approximated using second-order central finite differences.²⁷ Temporal integration of Eq. (1) was performed using the semi-implicit P2 projection scheme,²⁷ where the linear $(\nabla^2 \mathbf{u} - \gamma \mathbf{u})$ and nonlinear $(\mathbf{u} \cdot \nabla \mathbf{u})$ terms were discretized in time using second-order implicit Crank–Nicolson and explicit Adams–Bashforth methods, respectively. The P2 projection scheme ensures that the velocity field after each time step Δt is divergence free $(\nabla \cdot \mathbf{u} = 0)$, where Δt was chosen to satisfy the criterion $\max(\mathbf{u} \Delta t / \Delta x) \leq 0.5$. For all results reported in this study, Re was chosen as the control parameter, whereas $\beta = \pi/4$ and $\gamma = 63.67$ were held constant (see Ref. 28). Estimation of model parameters, including Re , from experimentally measurable quantities is detailed in the [supplementary material](#).

A. Forcing profiles

Let us recall that a lattice of nearly square vortices in experiments is generated using a chessboard-like array of magnets. In principle, the dimensions of such an array can be larger,⁶ smaller,²⁵ or equal²¹ to those of the flow domain. To ensure that forcing near the boundaries is nearly zero, we placed a magnet array with dimensions $(N_x - 2) \times (N_y - 2)$ inside each $N_x \times N_y$ domain, as shown in Fig. 1. Depending on whether N_x, N_y is even or odd, an integer or half-integer number of forcing wavelengths then fit into the flow domain along each spatial direction. Consequently, parities with respect to reflections in the x, y -axes for each forcing profile (listed in Table I) are distinct. Parity can also be inferred by approximating \mathbf{f} near the center of the flow domain as a product of sine/cosine functions. For instance, $\mathbf{f} \approx \cos(\pi x) \cos(\pi y) \hat{\mathbf{x}}$ in the 9×9 domain. Hence, the corresponding parity is even \times even.

While sinusoidal approximations of \mathbf{f} are convenient for analytical calculations,^{5,8,22} they fail to capture two important features of forcing profiles in experiments: (i) the aperiodic shape of the profile near

TABLE I. Forcing profile parities and sinusoidal approximations of \mathbf{f} ($\approx \tilde{f} \hat{\mathbf{x}}$) near the center of a flow domain. For a given profile, Eq. (1) is equivariant under the symmetries listed below. Dimensions of flow domains we analyzed are listed under the column $N_x \times N_y$. Prefixes/superscripts “ \pm ” indicate opposite directions of forcing.

Parity: $R_x \times R_y$	$\tilde{f}(x, y)$	Symmetries	$N_x \times N_y$
Even \times even	$\cos(\pi x) \cos(\pi y)$	R_y	9×9
Odd \times even	$\pm \sin(\pi x) \cos(\pi y)$	R_x, R_y, R_π	$10 \times 9^\pm$
Even \times odd	$\cos(\pi x) \sin(\pi y)$	R_π	9×10
Odd \times odd	$\sin(\pi x) \sin(\pi y)$	R_x	10×10

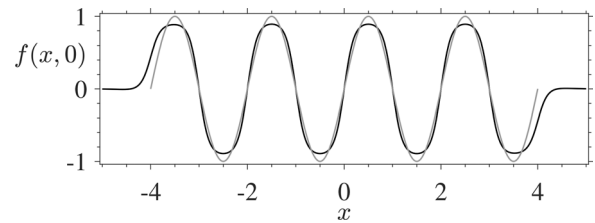


FIG. 2. Normalized forcing profile (black curve) along the cross section $y=0$ in the $10 \times 9^+$ domain (cf. Fig. 1). The gray curve is a sinusoidal fit $\tilde{f}(x, 0) = \sin(\pi x)$ estimated for $-2 \leq x \leq 2$.

the edges of a magnet array, and (ii) deviation from strict monochromaticity near the center, due to finite contributions from harmonics of the fundamental forcing wavelength. Previous studies^{21,25} have unambiguously validated the importance of accurately modeling these features to theoretically reproduce experimental flow patterns. Hence, we numerically computed the Q2D forcing profile by modeling the magnet array as a 3D lattice of dipoles. The 2D forcing profile \mathbf{f} was then computed using the depth-averaging procedure detailed in Ref. 25. For each domain listed in Table I, we normalized \mathbf{f} such that its sinusoidal fit $\tilde{f}(x, y) \hat{\mathbf{x}}$ near the center has unit amplitude, as shown in Fig. 2. Notice that the amplitude of the numerically computed profile is approximately 5% smaller than the leading sinusoidal mode $\sin(\pi x)$. This discrepancy can be reconciled by adding a correction term $0.05 \sin(3\pi x)$ to the analytical approximation $\tilde{f}(x, 0)$, which shows that the forcing profile in DNS is not monochromatic.

B. Linear stability analysis

The numerical integrator described above was also adapted to carry out linear stability analysis (LSA) of steady/equilibrium flows (\mathbf{u}_{eq}), to identify whether arbitrary infinitesimal perturbations $d\mathbf{u}$ to \mathbf{u}_{eq} would grow or decay with time. Toward this, we redefined $\mathbf{u} = \mathbf{u}_{eq} + d\mathbf{u}$ and recast Eq. (1) into the form $d\dot{\mathbf{u}} = \mathbf{F}(\mathbf{u}_{eq} + d\mathbf{u})$. Here, \mathbf{F} represents all terms in Eq. (1) excluding $\partial_t \mathbf{u}$. We then linearized \mathbf{F} about \mathbf{u}_{eq} ,

$$d\dot{\mathbf{u}} \approx \underbrace{\mathbf{F}(\mathbf{u}_{eq})}_{=0} + \mathbf{J}(\mathbf{u}_{eq}) d\mathbf{u}, \tag{2}$$

where $\mathbf{J} = \nabla_{\mathbf{u}} \mathbf{F}$ is the Jacobian matrix evaluated at \mathbf{u}_{eq} . The general solution $d\mathbf{u}(t)$ to the above equation can be expressed as a linear combination of the eigenvectors $\hat{\mathbf{e}}_k$ of \mathbf{J} as follows:

$$d\mathbf{u}(t) = \sum_k \varepsilon_k(t) \hat{\mathbf{e}}_k. \tag{3}$$

Henceforth, we refer to the eigenvectors/eigenvalues of the Jacobian matrix $\mathbf{J}(\mathbf{u}_{eq})$ simply as the eigenvectors/eigenvalues of \mathbf{u}_{eq} .

In Eq. (3), the evolution of each coefficient $\varepsilon_k(t) \approx \varepsilon_k(0) e^{\lambda_k t}$ is governed by the eigenvalue λ_k associated with $\hat{\mathbf{e}}_k$. Here, $\mathbf{J} \hat{\mathbf{e}}_k = \lambda_k \hat{\mathbf{e}}_k$ and $\varepsilon_k(0)$ defines the initial perturbation along $\hat{\mathbf{e}}_k$. If the largest real part $\sigma_1 = \max_k \Re(\lambda_k)$ of the eigenspectrum of \mathbf{u}_{eq} is negative, the magnitude $\|d\mathbf{u}\|$ of every infinitesimal perturbation decays to zero for $t \gg 1/|\sigma_1|$. A steady flow \mathbf{u}_{eq} is then linearly *stable*. In contrast, \mathbf{u}_{eq} is marginally (or neutrally) stable if $\sigma_1 = 0$, whereas it is linearly *unstable* if $\sigma_1 > 0$. Small perturbations along unstable eigendirections grow

exponentially over finite time intervals. For $t \rightarrow \infty$, however, their growth is bounded due to nonlinearity and dissipation. The saturation of amplitudes $\varepsilon_k(t \rightarrow \infty)$ then leads to the formation of new solutions in a bifurcation, that is, when σ_1 changes sign. Hence, to analyze the linear stability of a steady flow \mathbf{u}_{eq} and construct secondary solutions that emerge out of a bifurcation, we computed the leading eigenvalue and eigenvector of \mathbf{u}_{eq} using Arnoldi iteration.^{29,30}

III. SYMMETRIES OF THE GOVERNING EQUATION

In the limit of vanishing forcing ($\mathbf{f} \rightarrow 0$), Eq. (1) on a laterally bounded square/rectangular domain is equivariant (does not change in form) under the following coordinate transformations:

- $R_x(x, y) \rightarrow (-x, y)$: Reflection in $x = 0$,
- $R_y(x, y) \rightarrow (x, -y)$: Reflection in $y = 0$,
- $R_\pi(x, y) \rightarrow (-x, -y)$: Rotation by π about the origin.

Note that R_π is equivalent to combined reflections in the x and y axes, that is, $R_\pi = R_x R_y = R_y R_x$. The transformations of the velocity $\mathbf{u} = (u, v)$ and vorticity $\Omega(x, y) = (\nabla \times \mathbf{u}) \cdot \hat{\mathbf{z}}$ fields under R_x , R_y , and R_π are listed in Table II.

Parity of a forcing profile with respect to R_x , R_y , or R_π , which are collectively referred to as R in the following, however, can restrict the equivariance of Eq. (1). Since the profiles listed in Table I are either symmetric ($R\mathbf{f} = \mathbf{f}$) or antisymmetric ($R\mathbf{f} = -\mathbf{f}$) with respect to these twofold symmetries ($R^2 = I$), the governing equation takes the form

$$\frac{\partial \mathbf{u}}{\partial t} + \beta \mathbf{u} \cdot \nabla \mathbf{u} = -\nabla p + \frac{1}{Re} (\nabla^2 \mathbf{u} - \gamma \mathbf{u}) + (-1)^r \mathbf{f}, \quad (4)$$

under a transformation R , where $r = 0$ or 1 . For a particular combination of \mathbf{f} and R , Eq. (4) is identical to Eq. (1) if $r = 0$. Equation (1) with that forcing profile \mathbf{f} is then equivariant under R .

Symmetries of Eq. (1) for each forcing profile are listed in Table I, which shows that the governing equation is equivariant under R_x , R_y , and R_π only when the forcing profile parity is odd \times even. Furthermore, Eq. (1) is equivariant under only one or all three symmetries simultaneously, because R_x , R_y , and R_π are elements of the dihedral group D_2 with only two generators. As a result, each of these symmetries can be expressed as a product of the other two, for example, $R_y = R_x R_\pi = R_\pi R_x$.

Equivariance under a symmetry, however, does *not* imply that solutions of Eq. (1) are necessarily symmetry-invariant ($R\mathbf{u} = \mathbf{u}$); this has some important consequences. When a flow field \mathbf{u} is not R -invariant, the action of R on \mathbf{u} generates a dynamically equivalent symmetry-related copy $R\mathbf{u}$. On the other hand, if a steady flow \mathbf{u}_{eq} is invariant under a twofold symmetry R , its eigenvectors $\hat{\mathbf{e}}_k$ will be either R -symmetric or R -antisymmetric; that is, if $R\mathbf{u}_{eq} = \mathbf{u}_{eq}$, then $R\hat{\mathbf{e}}_k = \pm \hat{\mathbf{e}}_k$ (cf. Sec. III in Gibson *et al.*³¹). In addition, if \mathbf{u}_{eq} is invariant under R_x , R_y , as well as R_π , its eigenvectors cannot be

TABLE II. Transformation of velocity and vorticity fields under R_x , R_y , and R_π .

	R_x	R_y	R_π
$u(x, y) \rightarrow$	$-u(-x, y)$	$u(x, -y)$	$-u(-x, -y)$
$v(x, y) \rightarrow$	$v(-x, y)$	$-v(x, -y)$	$-v(-x, -y)$
$\Omega(x, y) \rightarrow$	$-\Omega(-x, y)$	$-\Omega(x, -y)$	$\Omega(-x, -y)$

antisymmetric with respect to all three symmetries. Hence, primary bifurcations in such flows may not break all symmetries simultaneously. As we shall see, identifying symmetries of both solutions and eigenvectors plays a crucial role in classifying bifurcations.

A. Invariance under $\mathbf{f} \rightarrow -\mathbf{f}$

Danilov *et al.*²¹ previously identified that a 2×2 lattice of rectangular vortices is not invariant under reversing the direction of forcing. From Eq. (4), we can see that $\mathbf{f} \rightarrow -\mathbf{f}$ is equivalent to a coordinate transformation R that is a broken symmetry of Eq. (1), that is, $r = 1$. Since a physical transformation cannot alter flow patterns and their dynamics, domains with a broken symmetry R are invariant under reversing the forcing direction. The exception is the odd \times even forcing case, where Eq. (1) is equivariant under R_x , R_y , and R_π . In the absence of a broken symmetry, the resulting flow patterns and dynamics should change when $\mathbf{f} \rightarrow -\mathbf{f}$. Indeed, the flow studied by Danilov *et al.*²¹ was driven by a forcing profile with an odd \times even parity, $\mathbf{f} \approx \sin(\pi x/2) \cos(\pi y)\hat{\mathbf{x}}$, which explains the observed sensitivity. In the present study, forcing with such a parity is realized in the $10 \times 9^\pm$ domains, where the \pm signs indicate opposite forcing directions.

We would like to highlight that previous experimental^{25,32,33} and numerical^{30,34,35} studies of the Kolmogorov flow, another canonical 2D flow driven by $\mathbf{f} = \sin(\pi y)\hat{\mathbf{x}}$ or $\cos(\pi y)\hat{\mathbf{x}}$, did not report the dynamical sensitivity discussed above. Such forcing profiles are generated in laboratory experiments using a one-dimensional array of rectangular magnets. The corresponding forcing profile parity is either even \times odd or even \times even, depending on whether an integer or half-integer number of forcing wavelengths fit in the y direction. The governing equation in both cases has a broken symmetry, which explains flow invariance when the direction of Kolmogorov forcing is reversed.

IV. THE SQUARE VORTEX FLOW

DNS of flow at low $O(1)$ Reynolds numbers converges to a chessboard-like lattice of nearly square vortices, independent of the forcing profile parity and direction. We refer to such a flow as the *primary solution* \mathbf{u}_0 of the governing equation. In the following, we focus on primary solutions in the $10 \times 9^\pm$ domains as representative examples, since they are not invariant under reversing the forcing direction.

In Fig. 3, panels (a) and (b) show primary solutions at $Re = 5$ in the $10 \times 9^+$ and $10 \times 9^-$ domains, respectively. Away from the boundaries, these flows are composed of a periodic arrangement of counter-rotating, nearly square vortices. The vortex centers align horizontally with those of the magnets, but are relatively shifted in the vertical direction by half the width of a magnet. Furthermore, these low- Re flows with opposite forcing directions can be approximately mapped to each other by merely flipping the sign of vorticity. This suggests that the transformations $\mathbf{f} \rightarrow -\mathbf{f}$ and $\mathbf{u} \rightarrow -\mathbf{u}$ leave the governing equation (almost) equivariant, which is the case if the flow is a (near) linear response to the forcing (cf. Ref. 36). Consequently, a chessboard-like lattice of square vortices near the center of the flow domain can be approximated as follows:

$$\tilde{\mathbf{u}}_0 = A\tilde{\mathbf{f}} \quad \text{and} \quad \tilde{v}_0 = A \partial_x \int \tilde{f} dy. \quad (5)$$

In the above equation, $\tilde{\mathbf{u}}_0 = [\tilde{u}_0, \tilde{v}_0]$ represents a sinusoidal velocity field driven by a strictly sinusoidal forcing $\mathbf{f} = \tilde{f}\hat{\mathbf{x}}$. $A(Re) \approx \pm Re/2\sqrt{2\pi^2 + \gamma}$ is the velocity amplitude computed using Eq. (1)

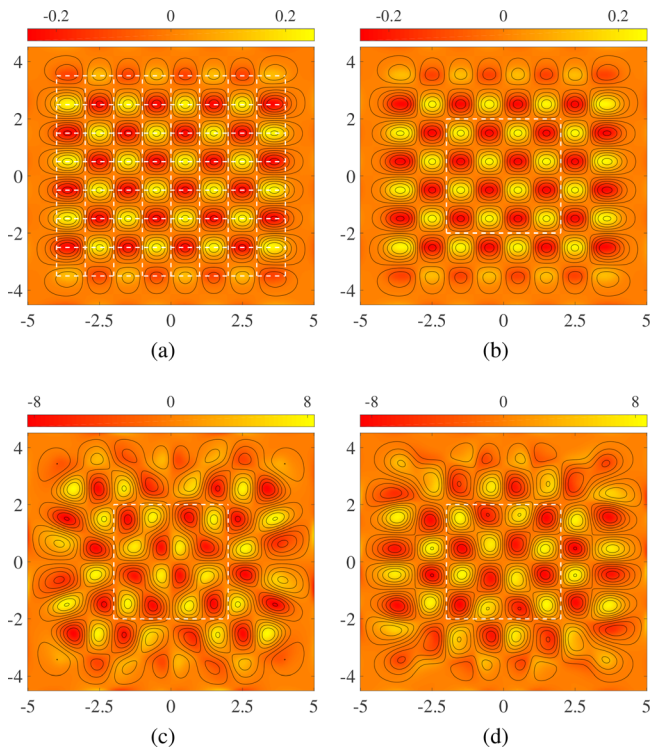


FIG. 3. Primary solutions \mathbf{u}_0 in the $10 \times 9^+$ (left column) and $10 \times 9^-$ (right column) domains at [(a) and (b)] $Re = 5$ and [(c) and (d)] $Re = 179$. Black curves indicate streamlines. Dashed white grid in panel (a) represents the magnet array. A sinusoidal flow model was tested inside the 4×4 square window marked in panels (b)–(d). All flow fields shown are symmetric with respect to R_x , R_y , and R_π . Color indicates vorticity $\Omega = (\nabla \times \mathbf{u}) \cdot \hat{z}$.

for opposite forcing directions. The analytical model $\tilde{\mathbf{u}}_0$, however, breaks down near the boundaries of the flow domain.

If the flow domain were of infinite lateral extent (without physical boundaries) and the forcing was strictly monochromatic, that is, $\mathbf{f} = \tilde{f}\hat{x}$, $\tilde{\mathbf{u}}_0$ would be an exact solution to Eq. (1) for all Re . In the present case, neither the forcing \mathbf{f} nor the square vortex flow it drives is strictly monochromatic. Due to coupling between different spatial frequencies, the shape and arrangement of vortices near the center of the domain undergo perceivable deformation as Re increases.²¹ The vortices near the lateral boundaries are also affected due to recirculating secondary flows. To illustrate these features, we plotted primary solutions at $Re = 179$ from the $10 \times 9^\pm$ domains in Figs. 3(c) and 3(d). Clearly, these two flows cannot be approximated using a simple linear model, unlike their low- Re counterparts. In addition, they are visually dissimilar, which confirms that flows in the $10 \times 9^\pm$ domains are not invariant under reversing the forcing direction.

To analyze the deformation of the square vortex flow, we computed the normalized difference Δ_l between \mathbf{u}_0 in DNS and its sinusoidal approximation $\tilde{\mathbf{u}}_0$ with increasing Re . Here

$$\Delta_l = \frac{\|\mathbf{u}_0 - \tilde{\mathbf{u}}_0\|}{\|\mathbf{u}_0\|}. \tag{6}$$

In the above equation, $\|\cdot\|$ represents L_2 -norm evaluated inside a 4×4 square region near the center of the flow domain, as indicated in Fig. 3. The plot of Δ_l vs Re in Fig. 4(a) (Multimedia view) reveals two different regions. For $Re \leq 120$, the difference between \mathbf{u}_0 and $\tilde{\mathbf{u}}_0$ is small and nearly constant at approximately 10%. Flow near the center indeed resembles a chessboard-like lattice of square vortices for these Re . When the Reynolds number increases above $Re \approx 120$, however, Δ_l increases steeply indicating rapid deformation of the square vortex flow. To illustrate the same, multimedia view associated with Fig. 4(a) shows side-by-side co-evolving plots of \mathbf{u}_0 and Δ_l at several $Re \leq 180$ in the $10 \times 9^+$ domain. Finally, even though we presented results only for the $10 \times 9^\pm$ domains here, square vortex flows in other domains we analyzed also begin to deform at $Re \approx 120$.

Sharp increase in Δ_l raises the question whether primary solutions in the $10 \times 9^\pm$ domains turn unstable at $Re \approx 120$. To test this, we computed their leading eigenvalues and found that these primary solutions remain stable up to $Re \approx 180$, much beyond the onset of deformation [cf. Fig. 4(b)]. These findings highlight that lateral confinement and the forcing profile affect flow patterns even at moderately high Re . We would like to note that Danilov *et al.*²¹ previously studied the deformation of a rectangular vortex flow. However, branch continuation (cf. see Appendix B) and linear stability analysis were not employed to validate that the observed deformation was not due to an instability. Finally, Fig. 4 reveals that deformation and stability of square vortex flows in the $10 \times 9^\pm$ domains are quantitatively different, which demonstrates these flows are also dynamically dissimilar.

The primary solution \mathbf{u}_0 in each $N_x \times N_y$ domain listed in Table I is invariant under all symmetries of the corresponding governing equation, regardless of Re . For instance, \mathbf{u}_0 in the $10 \times 9^\pm$ domains is invariant under R_x , R_y , and R_π (cf. Fig. 3). In contrast, \mathbf{u}_0 in the 9×10 domain is invariant only under R_π [cf. Fig. 7(a)]. Similarly, primary solutions in the 9×9 and 10×10 domains shown in Fig. 9 are R_y -invariant and R_x -invariant, respectively. Secondary solutions that branch out of \mathbf{u}_0 in each of these domains, however, need not be symmetry invariant. We explore this aspect in Sec. V.

V. SYMMETRY-BREAKING PRIMARY BIFURCATIONS

Using linear stability analysis, we can detect whether the square vortex flow turns unstable to infinitesimal perturbations. However, we

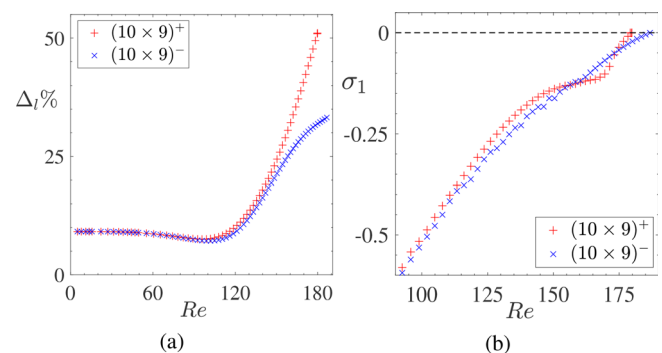


FIG. 4. Spatial deformation and linear stability of primary solutions \mathbf{u}_0 in the $10 \times 9^\pm$ domains. (a) Normalized difference Δ_l between \mathbf{u}_0 in DNS and its sinusoidal approximation $\tilde{\mathbf{u}}_0$. (b) Real part σ_1 of the leading eigenvalue of \mathbf{u}_0 . Multimedia view: <https://doi.org/10.1063/5.0061658.1>

cannot definitively predict whether secondary solutions that emerge due to an instability are steady or time-dependent, for example, chaotic.^{12,21} Also, LSA cannot reveal whether the transition to a secondary solution will be supercritical or subcritical. Given the multitude of possibilities, we structure the following discussion based on various types of symmetry-breaking bifurcations we identified in the DNS. In addition, we group different $N_x \times N_y$ domains that undergo a specific bifurcation and analyze a representative example in detail.

A. Supercritical pitchfork bifurcations

We start our analysis with the $10 \times 9^+$ domain, where the primary solution \mathbf{u}_0 undergoes an instability at $Re_{p1} = 179.81$, when its leading real eigenvalue changes sign (cf. Figs. 3 and 4). The corresponding eigenvector,³⁷ shown in Fig. 5(a), is R_y -symmetric and R_x, R_π -antisymmetric. We found that DNS of flow slightly above Re_{p1} converges to either of the steady solutions \mathbf{u}_1^\pm , which are invariant only under R_y . As an example, Fig. 5(b) shows \mathbf{u}_1^+ at $Re = 188.4$, well above the bifurcation point. Also, \mathbf{u}_1^+ and \mathbf{u}_1^- are related to each other via the symmetries $R \in \{R_x, R_\pi\}$ broken in the bifurcation, that is, $R\mathbf{u}_1^+ = \mathbf{u}_1^\mp$. Hereafter, we distinguish such symmetry-related solutions using superscripts “ \pm .” The formation of two secondary solution branches with a broken symmetry confirms that \mathbf{u}_0 in the $10 \times 9^+$ domain undergoes a *pitchfork* bifurcation at Re_{p1} .

To quantitatively analyze this bifurcation, we computed the normalized separation Δ_1^\pm between \mathbf{u}_0 and \mathbf{u}_1^\pm at several Reynolds numbers above the bifurcation point, where

$$\Delta_1^\pm = \pm \frac{\|\mathbf{u}_1^\pm - \mathbf{u}_0\|}{\|\mathbf{u}_{0c}\|}. \tag{7}$$

In the above equation, $\|\cdot\|$ represents L_2 -norm evaluated over the entire flow domain and \mathbf{u}_{0c} is the neutrally stable primary solution at Re_{p1} . For completeness, we also defined $\Delta_0 = 0$ as the order parameter representing \mathbf{u}_0 . In Fig. 6, we plotted Δ_0 and Δ_1^\pm vs Re to visualize the primary bifurcation in the $10 \times 9^+$ domain. Clearly, Δ_1^\pm is zero at Re_{p1} and increases continuously with $Re \geq Re_{p1}$, which confirms a *supercritical* transition from \mathbf{u}_0 to \mathbf{u}_1^\pm .

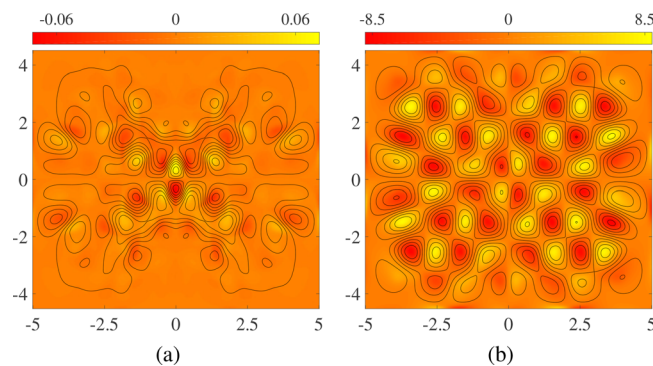


FIG. 5. Primary instability and secondary solution \mathbf{u}_1^+ in the $10 \times 9^+$ domain. (a) Leading eigenvector $\hat{\mathbf{e}}_1$ of the primary solution \mathbf{u}_0 that turns unstable at $Re_{p1} = 179.81$. $\hat{\mathbf{e}}_1$ is R_y -symmetric and R_x, R_π -antisymmetric. (b) R_y -invariant secondary solution \mathbf{u}_1^+ at $Re = 188.4$. Symmetries of \mathbf{u}_1^+ can be inferred from the vortex pattern near the center. \mathbf{u}_1^- is the reflection of \mathbf{u}_1^+ in the y -axis.

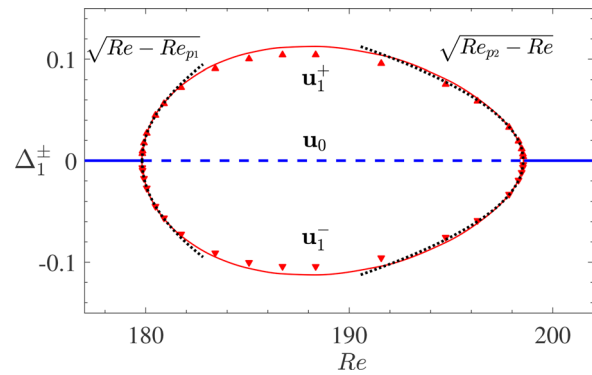


FIG. 6. Supercritical pitchfork bifurcations of the primary solution \mathbf{u}_0 in the $10 \times 9^+$ domain. Secondary solutions \mathbf{u}_1^\pm (red curves) emerge out of a forward pitchfork bifurcation at $Re_{p1} = 179.81$ and disappear through a backward pitchfork bifurcation at $Re_{p2} = 198.56$. Solid and dashed curves represent linearly stable and unstable solutions, respectively. Up/down triangles indicate saturated amplitudes $\pm \varepsilon$ along the unstable eigenvector of \mathbf{u}_0 . Dotted black curves indicate square root scaling of ε near Re_{p1} and Re_{p2} .

Infinitesimally close to the critical Re , the pitchfork solutions are formed due to nonlinear saturation of the primary instability. Hence, \mathbf{u}_1^\pm can be approximated^{1,2} as

$$\mathbf{u}_1^\pm = \mathbf{u}_0 \pm \varepsilon \|\mathbf{u}_{0c}\| \hat{\mathbf{e}}_1. \tag{8}$$

Since $R\hat{\mathbf{e}}_1 = -\hat{\mathbf{e}}_1$ for $R \in \{R_x, R_\pi\}$, it is straightforward to show using the above equation that $R\mathbf{u}_1^\pm = \mathbf{u}_1^\mp$, that is, symmetries broken via the pitchfork bifurcation map the resulting secondary solutions to each other and render them dynamically equivalent at all Re .

It is not known *a priori*, however, whether Eq. (8) is quantitatively accurate at a finite distance above the bifurcation point. To test this, we computed the amplitude ε using the relation

$$\varepsilon = \frac{\|(\mathbf{u}_1^\pm - \mathbf{u}_0) \cdot \hat{\mathbf{e}}_1\|}{\|\mathbf{u}_{0c}\|}. \tag{9}$$

We then compared $\pm \varepsilon$ and Δ_1^\pm at several $Re \geq Re_{p1}$. We recall that Δ_1^\pm is the normalized magnitude of the vector $\mathbf{u}_1^\pm - \mathbf{u}_0$, whereas ε is the magnitude of its projection along $\hat{\mathbf{e}}_1$. As a result, $\varepsilon \leq |\Delta_1^\pm|$ and the equality is satisfied only if $\mathbf{u}_1^\pm - \mathbf{u}_0$ is parallel to $\hat{\mathbf{e}}_1$. Figure 6 shows that $\pm \varepsilon$ (up/down triangles) and Δ_1^\pm are practically indistinguishable inside a narrow interval of Re (of width $\Delta Re \approx 2$) near the bifurcation point. Inside this window, the Reynolds number dependence of ε satisfies the square root scaling^{1,2} remarkably accurately (dotted black curve), that is, $\varepsilon \propto \sqrt{Re - Re_{p1}}$. These findings confirm that Eq. (8) is indeed quantitatively accurate close to the bifurcation.

Figure 6 also shows that Δ_1^\pm and ε are comparable in magnitude even farther away from the bifurcation point, where they cease to vary monotonically with Re . This implies $\mathbf{u}_1^\pm - \mathbf{u}_0$ and $\hat{\mathbf{e}}_1$ are almost parallel at these Re , and Eq. (8) should still reliably approximate the pitchfork branches. This observation enabled us to rationalize differences between solutions \mathbf{u}_1^\pm and \mathbf{u}_0 in physical space. These solutions differ appreciably only near the center of the flow domain due to the corresponding localization of $\hat{\mathbf{e}}_1$ (cf. Fig. 3 vs Fig. 5). We would like to note that a similar “visual” approach was previously employed by Thess⁵ to theoretically analyze experimentally observed¹² pitchfork bifurcation

in a 2×2 lattice of square vortices. Secondary solutions, which emerge due to the merger of diagonally opposite vortices, were constructed using an equation analogous to Eq. (8), however, by choosing an arbitrary amplitude ε along $\pm \hat{e}_1$ [cf. Eq. (21) in Theiss⁵]. Recently, Chen⁸ also showed that supercritical pitchfork states reported in Sommeria¹² can be analytically approximated using a truncated model with only four sinusoidal modes. These studies, however, employed free-slip boundary conditions and a monochromatic sinusoidal forcing.

The pitchfork bifurcation at Re_{p1} is a symmetry-breaking one, since the secondary solutions \mathbf{u}_1^\pm are not R_x, R_π -invariant. Typically, these solutions should become unstable at higher Re , resulting in tertiary solutions with greater spatial asymmetry and/or temporal complexity. In the present case, however, we found that both \mathbf{u}_1^\pm coalesce with the unstable primary solution \mathbf{u}_0 at $Re_{p2} = 198.56$ in a *backward* supercritical pitchfork bifurcation,³⁸ as shown in Fig. 6. At this Reynolds number, \mathbf{u}_0 regains stability with respect to perturbations along the leading eigenvector \hat{e}_1 , which is R_y -symmetric and R_x, R_π -antisymmetric. Consequently, the flow in DNS regains all its symmetries for $Re > Re_{p2}$.

When continued to higher Re , \mathbf{u}_0 in the $10 \times 9^+$ domain becomes unstable again at $Re = 208.79 > Re_{p2}$. Before we discuss this instability, we compare primary bifurcations in the $10 \times 9^\pm$ domains when the forcing direction is reversed. \mathbf{u}_0 in the $10 \times 9^-$ domain turns unstable when a complex-conjugate pair of eigenvalues crosses the imaginary axis, which presents a different scenario than a pitchfork bifurcation. However, it is not surprising that the nature of primary bifurcations in $10 \times 9^\pm$ domains is different, since the corresponding primary solutions are dynamically dissimilar (cf. Figs. 3 and 4). We shall revisit bifurcations in the $10 \times 9^\pm$ domains again in Secs. V C and VI.

B. Subcritical pitchfork and saddle-node bifurcations

In a supercritical bifurcation, the transition from primary to secondary solutions near the bifurcation point is continuous, as shown in Fig. 6. However, for a given bifurcation type (e.g., the pitchfork), the square vortex flow can also undergo a discontinuous/sudden transition upon increasing the Reynolds number only infinitesimally above a critical value. In this section, we explore one such example from the 9×10 domain. This domain is identical to the $10 \times 9^+$ one shown in Fig. 1, except that $J\hat{y} \rightarrow J\hat{x}$.

The primary solution \mathbf{u}_0 in the 9×10 domain is R_π -invariant, as shown in Fig. 7(a). At $Re_{p1} = 189.99$, \mathbf{u}_0 turns unstable to perturbations along a real R_π -antisymmetric eigenvector \hat{e}_1 . DNS of flow slightly above the bifurcation converges to either of the stable R_π -asymmetric solutions \mathbf{u}_4^\pm that map to each other via the broken symmetry, that is, $\mathbf{u}_4^- = R_\pi \mathbf{u}_4^+$. Unlike in the supercritical case, however, these solutions lie “far” away from \mathbf{u}_0 . For instance, Fig. 7(b) shows \mathbf{u}_4^+ , that is visibly distinct from \mathbf{u}_0 computed at the same Re . The loss of R_π -invariance and a sudden transition from \mathbf{u}_0 to either of the symmetry-related solutions \mathbf{u}_4^\pm suggests that the stable primary solution in the 9×10 domain undergoes a *subcritical pitchfork* bifurcation at Re_{p1} .

To analyze the sudden transition, we defined the following order parameter to quantify the separation between \mathbf{u}_0 and a solution pair \mathbf{u}_k^\pm (labeled using subscript k) at each Re :

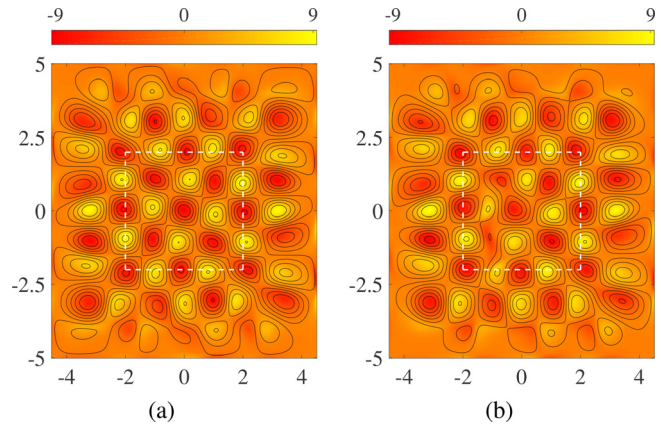


FIG. 7. Steady flows in the 9×10 domain at $Re = 189.99$. (a) R_π -invariant primary solution \mathbf{u}_0 . (b) Asymmetric flow \mathbf{u}_4^+ resulting from a subcritical pitchfork bifurcation. These flows differ noticeably near the bottom left corner of the square marked using dashed white lines.

$$\Delta_k^\pm = \pm \frac{\|\mathbf{u}_k^\pm - \mathbf{u}_0\|}{\|\mathbf{u}_{0c}\|}. \quad (10)$$

In the above equation, \mathbf{u}_{0c} is the neutrally stable primary solution at Re_{p1} . Figure 8 quantifies the variation of Δ_k^+ corresponding to \mathbf{u}_4^+ , as well as other branches, as a function of Re . Curves representing \mathbf{u}_k^- are not shown in this figure, since they can be reconstructed using the

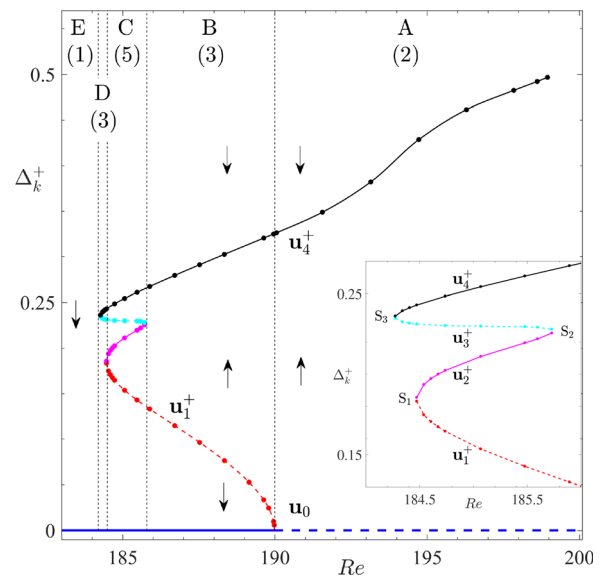


FIG. 8. Subcritical pitchfork and saddle-node bifurcations in the 9×10 domain. Stable solutions (\mathbf{u}_0 for $Re < Re_{p1}$, \mathbf{u}_2^+ , and \mathbf{u}_4^+) are represented using solid curves (see inset). Unstable solutions (\mathbf{u}_0 for $Re > Re_{p1}$, \mathbf{u}_1^+ , and \mathbf{u}_3^+) are represented using dashed curves. Regions between vertical dashed lines mark intervals of multi-stability, labeled A through E. Number of stable solutions in each interval is shown in parenthesis. The solution branches \mathbf{u}_k^- are not plotted, but can be reconstructed using the relation $\Delta_k^- = -\Delta_k^+$. Vertical arrows indicate basins of attractions for various branches.

relation $\Delta_k^- = -\Delta_k^+$. Clearly, \mathbf{u}_4^+ is always disconnected from \mathbf{u}_0 (represented by $\Delta_0 = 0$) by a finite amplitude. However, since \mathbf{u}_0 is unstable for $Re > Re_{p1}$, DNS of flow starting from initial conditions $\mathbf{u} \approx \mathbf{u}_0$ eventually converges to \mathbf{u}_4^+ , as indicated by the arrow. This explains the sudden transition from \mathbf{u}_0 to \mathbf{u}_4^+ upon infinitesimally increasing the Reynolds number above Re_{p1} .

In a subcritical pitchfork bifurcation, two *unstable* symmetry-related solutions \mathbf{u}_1^\pm exist for $Re < Re_{p1}$, which then coalesce with \mathbf{u}_0 at the critical Reynolds number Re_{p1} (red dashed curve in Fig. 8). Despite similarity in shape with a backward supercritical pitchfork bifurcation (Sec. V A), \mathbf{u}_1^\pm in the subcritical case are unstable and cannot be computed using mere numerical integration. Nevertheless, \mathbf{u}_1^\pm can be approximated using Eq. (8) by redefining \mathbf{u}_0 as the stable primary solution for $Re < Re_{p1}$, $\hat{\mathbf{e}}_1$ as the leading stable eigenvector of \mathbf{u}_0 , and ε as the *a priori* unknown amplitude of the pitchfork branches. To compute \mathbf{u}_1^\pm accurately, we generated initial conditions $\mathbf{u}_1^\pm(\tilde{\varepsilon}) = \mathbf{u}_0 \pm \tilde{\varepsilon} \|\mathbf{u}_0\| \hat{\mathbf{e}}_1$ parameterized by $\tilde{\varepsilon}$ and employed the Newton solver discussed in Appendix A. The solver successfully converged to \mathbf{u}_1^\pm when $\tilde{\varepsilon} \approx \varepsilon$, the saturated amplitude along $\hat{\mathbf{e}}_1$.

One may now ask, what is the relation between the stable finite-amplitude solution \mathbf{u}_4^+ observed for $Re > Re_{p1}$ and the unstable pitchfork branch \mathbf{u}_1^+ computed for $Re < Re_{p1}$ in Fig. 8? In the simplest possible scenario, \mathbf{u}_1^+ and \mathbf{u}_4^+ are born out of a *saddle-node* bifurcation at a subcritical Reynolds number $Re_{sn} < Re_{p1}$. In such a bifurcation, two solutions that differ in the number of unstable directions by unity collide and annihilate each other.^{3,39} To test this, we continued both \mathbf{u}_1^+ and \mathbf{u}_4^+ to lower Re using the parabolic extrapolation technique detailed in Appendix B, until a change in stability of each solution was detected. We found that \mathbf{u}_1^+ and \mathbf{u}_4^+ “snake” around and annihilate intermediate solution branches \mathbf{u}_2^+ (stable) and \mathbf{u}_3^+ (unstable), respectively. These solutions emerge in a sequence of three saddle-node⁴⁰ bifurcations S_1, S_2 , and S_3 , as shown in Fig. 8.

The subcritical transition in Fig. 8 is significantly more complicated than its supercritical counterpart shown in Fig. 6. Particularly, the stability scenarios in Fig. 8 are intricate, which we discuss in the following. To distinguish various intervals of multi-stability, we marked all bifurcation points in Fig. 8 using vertical dashed lines and labeled the intervals between them (A through E). The number of stable solutions within each interval, including the \mathbf{u}_k^- branches not shown, is also indicated in parenthesis. Figure 8 shows that two stable branches are always separated by an unstable branch. For instance, the unstable section of the \mathbf{u}_0 branch serves as a separatrix between \mathbf{u}_4^+ and \mathbf{u}_4^- inside the interval A, which explains why DNS of flow starting from $\mathbf{u} \approx \mathbf{u}_0$ converges to \mathbf{u}_4^+ for $Re > Re_{p1}$. Inside the interval B, the stable branches \mathbf{u}_4^+ (\mathbf{u}_4^-) and \mathbf{u}_0 are separated by the unstable branch \mathbf{u}_1^+ (\mathbf{u}_1^-). In this interval, DNS of flow starting from arbitrary initial conditions converges to \mathbf{u}_0 or \mathbf{u}_4^\pm . Interval C is a striking example of multi-stability, with five stable solutions (to which the DNS converges) and four unstable ones that serve as separatrices between the former. Finally, the stability scenario inside the narrow interval D, with stable solutions \mathbf{u}_4^\pm , \mathbf{u}_0 and the unstable pair \mathbf{u}_3^\pm , is qualitatively similar to that in interval B. This can also be visualized from the inset in Fig. 8.

Subcritical transition in a 6×6 lattice of nearly square Q2D vortices was previously observed in experiments due to Sommeria (cf. Fig. 2 in Ref. 12). Beyond a critical Reynolds number, the author found that the steady square vortex flow suddenly transitions to a finite-amplitude chaotic solution. Upon decreasing the Reynolds number, an

intermediate stable equilibrium state was identified within a narrow interval of Re . With further decrease in Re , the stable square vortex flow was found to reappear in a sudden transition. Even though unstable branches cannot be realized in experiments, we conjecture that the above described bifurcation is similar to that shown in Fig. 8. In fact, we can qualitatively compare both transition scenarios by invoking the following mapping: \mathbf{u}_0 in Fig. 8 maps to the 6×6 lattice of square vortices, and \mathbf{u}_4^+ represents the disconnected chaotic solution, whereas \mathbf{u}_2^+ is the intermediate state. Even though direct transition to chaos is not observed in our study, such a transition can occur if \mathbf{u}_4^\pm turn unstable soon after they are born.⁴¹ Nevertheless, since the experimental setup employed by Sommeria is markedly different from that modeled in the present study (the forcing profile, domain size, and frictional drag), quantitative differences between the two are expected.

We conclude our analysis of the subcritical pitchfork bifurcation with a short discussion on the symmetries of various solution branches in Fig. 8. To begin, the solutions \mathbf{u}_1^\pm are not invariant under R_π , the symmetry broken in the bifurcation. In addition, we found that the asymmetry of \mathbf{u}_1^\pm , quantified as $\|\mathbf{u}_1^\pm - R_\pi \mathbf{u}_1^\pm\| / \|\mathbf{u}_1^\pm\|$, increases with the distance $\|Re - Re_{p1}\|$ from the bifurcation point. This implies that both \mathbf{u}_1^+ and \mathbf{u}_2^+ are born with a finite R_π asymmetry at the saddle-node bifurcation S_1 . We also found that \mathbf{u}_2^+ , \mathbf{u}_3^+ , and \mathbf{u}_4^+ are finitely R_π -asymmetric at all Reynolds numbers these solutions exist. In addition, \mathbf{u}_0 undergoes further bifurcations at higher Re and does not regain its stability, at least in the range of Re values we explored. Hence, the subcritical pitchfork bifurcation leads to the breaking of the only flow symmetry R_π in the 9×10 domain.

C. Supercritical Hopf bifurcation

Pitchfork bifurcations discussed in Secs. V A and V B have led to the formation of steady secondary solutions. However, bifurcations in a square vortex flow can also lead to the direct onset of time-periodic dynamics.²⁰ We found such flow transitions in the 9×9 , 10×10 , and $10 \times 9^-$ domains (cf. Figs. 3 and 9). Flow in the $10 \times 9^+$ domain, where the primary solution \mathbf{u}_0 regains stability via the backward pitchfork bifurcation, also becomes time-periodic at $Re_{h1} > Re_{p2}$. Using linear stability analysis and numerical integration, we identified that \mathbf{u}_0

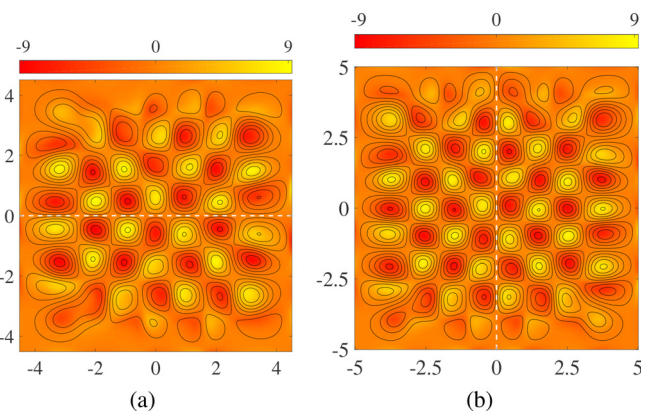


FIG. 9. Primary solutions in the (a) 9×9 domain at $Re = 190.97$ (b) 10×10 domain at $Re = 177.98$. Dashed white lines indicate invariance under symmetries (a) R_y and (b) R_x .

in each of these domains undergoes a *supercritical Hopf* bifurcation (cf. Table III). At the critical Reynolds number Re_{h1} , real part of the leading complex-conjugate eigenvalue pair of \mathbf{u}_0 changes sign. Since the dynamics above onset of oscillations are qualitatively similar across various flow domains, we focus on the 9×9 domain as a representative example due to symmetry considerations.

The primary solution \mathbf{u}_0 in the 9×9 domain is R_y -invariant, as shown in Fig. 9(a). Slightly above $Re_{h1} = 190.97$, DNS of flow converges to a stable time-periodic solution $\mathbf{u}_{po1}(t)$. The period of oscillations $T \approx 2\pi/\omega_{1c}$ was estimated using the Newton solver,⁴² such that $\|\mathbf{u}_{po1}(t) - \mathbf{u}_{po1}(t + T)\| \leq 10^{-8}$ for $t \in (0, T]$. Here, ω_{1c} is the imaginary part of the leading eigenvalue of \mathbf{u}_0 at the critical Reynolds number Re_{h1} . To test whether the bifurcation is supercritical or subcritical, we computed the normalized maximum separation

$$\Delta_{po1} = \max_t \frac{\|\mathbf{u}_{po1}(t) - \mathbf{u}_0\|}{\|\mathbf{u}_{0c}\|} \quad (11)$$

between the solution branches \mathbf{u}_0 and \mathbf{u}_{po1} for $Re > Re_{h1}$. We found that Δ_{po1} vanishes near the bifurcation point, confirming a supercritical transition.

Infinitesimally close to the onset of oscillations, the secondary solution \mathbf{u}_{po1} formed via the supercritical Hopf bifurcation can be approximated as

$$\mathbf{u}_{po1}(t) = \mathbf{u}_0 + \|\mathbf{u}_{0c}\| [p_1(\omega t)\hat{\mathbf{w}}_1 + p_2(\omega t)\hat{\mathbf{w}}_2]. \quad (12)$$

Here, $\omega = 2\pi/T$ is the angular frequency of oscillations and $\hat{\mathbf{w}}_1, \hat{\mathbf{w}}_2$ are mutually orthonormal vectors in a plane spanned by the real and imaginary parts of $\hat{\mathbf{e}}_1^\pm = \mathbf{e}_r \pm i\mathbf{e}_c$, the unstable eigenvectors of \mathbf{u}_0 . Coefficients p_1 and p_2 are projections of $\mathbf{u}_{po1}(t) - \mathbf{u}_0$ along $\hat{\mathbf{w}}_1$ and $\hat{\mathbf{w}}_2$, respectively. Furthermore, p_1 and p_2 satisfy the relation $p_{1,2}(t + T) = p_{1,2}(t) \forall t$, since \mathbf{u}_{po1} is time-periodic. Using Eq. (12), we defined the amplitude of oscillations as

$$A = \max_t \sqrt{p_1^2 + p_2^2}. \quad (13)$$

Infinitesimally close to the bifurcation point, A should scale¹⁻³ with Reynolds number as $A \propto \sqrt{Re - Re_{h1}}$. In contrast, the angular frequency ω is supposed to scale linearly with Re , that is, $\omega - \omega_{1c} \propto Re - Re_{h1}$. Below, we test the accuracy of Eq. (12) and these scaling laws, following an approach similar to that employed in Sec. V A.

Equation (12) implies that the evolution of \mathbf{u}_{po1} around \mathbf{u}_0 is confined to the $\hat{\mathbf{w}}_1 - \hat{\mathbf{w}}_2$ plane. To visualize the dynamics in this plane,

TABLE III. Hopf bifurcations of square vortex flows in different $N_x \times N_y$ domains. Re_{h1} is the critical Reynolds number for the onset of oscillations with period $T = 2\pi/\omega_{1c}$. The union of symmetries broken via the Hopf bifurcation and symmetries of the resulting \mathbf{u}_{po1} is the full set of symmetries for each flow domain. Each time-periodic solution is stable inside the interval $Re_{h1} < Re < Re_2$.

$N_x \times N_y$	Re_{h1}	T	Symmetry broken	Invariance	Re_2
9×9	190.97	16.57	R_y	None	194.6
$10 \times 9^+$	208.79	15.75	R_y, R_π	R_x	210.1
$10 \times 9^-$	186.76	16.39	R_x, R_y	R_π	194.9
10×10	177.98	50.11	None	R_x	178.8

we plotted $p_1(t)$ vs $p_2(t)$ in Fig. 10(a). Here, each elliptical orbit represents \mathbf{u}_{po1} at a particular Reynolds number $Re > Re_{h1}$, whereas center $(0, 0)$ represents the unstable primary solution \mathbf{u}_0 (for all Re). For convenience, we also defined $\hat{\mathbf{w}}_1$ such that the intersection of each orbit with the p_1 -axis is equal to the amplitude A of oscillations. Now, if the evolution of a time-periodic orbit \mathbf{u}_{po1} is indeed confined to the $\hat{\mathbf{w}}_1 - \hat{\mathbf{w}}_2$ plane, the corresponding amplitude in Fig. 10(a) should be equal to Δ_{po1} (+ symbols), the maximum separation between \mathbf{u}_{po1} and \mathbf{u}_0 .

Figure 10(a) shows that A and Δ_{po1} are indistinguishable for the three innermost orbits, which lie inside a narrow interval of Reynolds numbers $0 < Re - Re_{h1} < 1$ near the bifurcation point. Inside this interval, the amplitude A and angular frequency ω of oscillations obey the square root and linear scaling laws, respectively, as shown in Figs. 10(b) and 10(c). The corresponding fits (dashed curves) are computed only for $0 < Re - Re_{h1} < 1$, to demonstrate that $A(Re)$ and $\omega(Re)$ deviate appreciably from theoretical predictions farther away from the bifurcation point. Nevertheless, our results show that time-periodic flows that emerge due to a supercritical Hopf bifurcation in the square vortex flow are accurately modeled by Eq. (12), however, only very close to the bifurcation point.

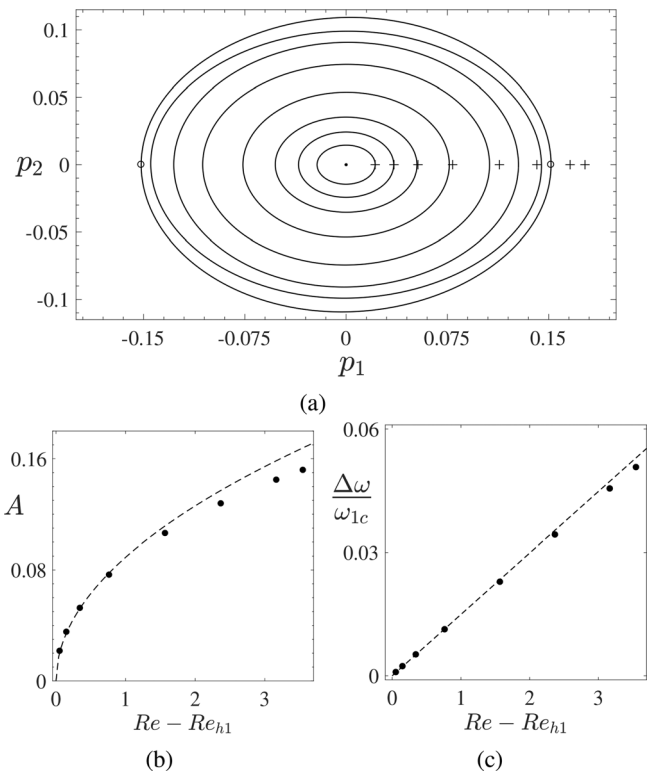


FIG. 10. Supercritical Hopf bifurcation in the 9×9 domain resulting in a time-periodic solution \mathbf{u}_{po1} . (a) Phase portraits of \mathbf{u}_{po1} at eight different Reynolds numbers inside the interval $Re_{h1} < Re < Re_2$. The semi-major axis A of each elliptical orbit and Δ_{po1} (+ symbols) increase with $Re - Re_{h1}$. Open circles on the outermost orbit represent flow snapshots in Fig. 11. (b) Square root scaling of the amplitude A and (c) linear scaling of the frequency of oscillations $\Delta\omega = \omega - \omega_{1c}$ above the critical Reynolds number Re_{h1} .

Unlike the pitchfork bifurcation, a supercritical Hopf is not consistently a symmetry-breaking bifurcation.^{25,43,44} In the present case, if the primary solution turns unstable to perturbations in the plane spanned by an R -symmetric complex-conjugate eigenvector pair $\hat{\mathbf{e}}_1^\pm$, the resulting time-periodic flow \mathbf{u}_{po1} will be R -invariant. This can be deduced from Eq. (12), since $R\hat{\mathbf{e}}_1^\pm = \hat{\mathbf{e}}_1^\pm$ implies $R\hat{\mathbf{w}}_{1,2} = \hat{\mathbf{w}}_{1,2}$. In contrast, if $\hat{\mathbf{e}}_1^\pm$ is R -antisymmetric, then \mathbf{u}_{po1} will not be R -invariant. Across the various flow domains we explored, a fully asymmetric time-periodic secondary solution is observed only in the 9×9 domain, where the R_y symmetry is broken. On the other hand, no symmetry is broken via the Hopf bifurcation in the 10×10 domain. We recall that $\hat{\mathbf{e}}_1^\pm$ cannot be simultaneously antisymmetric with respect to R_x, R_y , as well as R_π in the $10 \times 9^\pm$ domains. Consequently, symmetry-breaking supercritical Hopf bifurcations in these domains lead to the formation of time-periodic flows that are invariant under exactly one symmetry of the governing equation, as listed in Table III.

When a twofold symmetry R is broken via a supercritical Hopf bifurcation, the resulting time-periodic flow \mathbf{u}_{po1} satisfies the relation^{33,43}

$$R\mathbf{u}_{po1}(t) = \mathbf{u}_{po1}(t + T/2), \tag{14}$$

which also leads to $\mathbf{u}_{po1}(t) = \mathbf{u}_{po1}(t + T)$, since $R^2 = I$. A solution to the governing equation, which satisfies the above relation, is termed a ‘‘pre-periodic’’ orbit⁴⁵ (PPO). Equation (14) implies that, two flow fields on \mathbf{u}_{po1} , which are separated in time by $T/2$, are related to each other via the twofold symmetry broken in the Hopf bifurcation. To visualize this, Fig. 11 (Multimedia view) shows flow snapshots on \mathbf{u}_{po1} from the 9×9 domain at instants marked using the open circles in Fig. 10(a). These R_y -asymmetric flows can be mapped to each other via R_y , the symmetry broken in the Hopf bifurcation. We note that PPOs are also formed in the $10 \times 9^\pm$ domains. However, they are invariant under one of the symmetries of Eq. (1). One important consequence of Eq. (14) is that spatially averaged instantaneous kinetic energy for PPOs oscillates at twice the frequency compared to kinetic energy measured at an arbitrary location in the flow. This feature distinguishes PPOs from merely time-periodic solutions (see the supplementary material video 1).

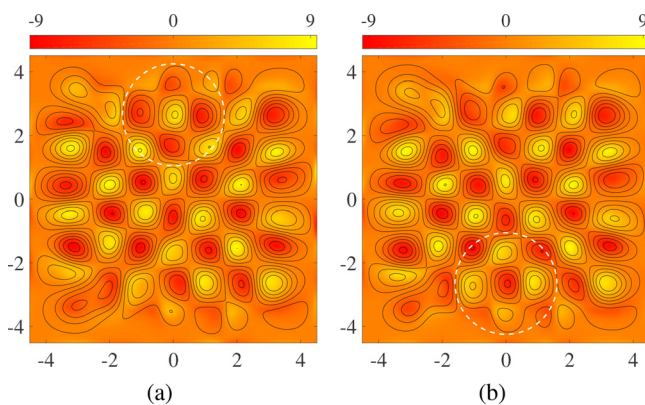


FIG. 11. Pre-periodic flows at $Re = 194.51$ that emerge out of a symmetry-breaking Hopf bifurcation in the 9×9 domain. (a) $\mathbf{u}_{po1}(t)$ and (b) $\mathbf{u}_{po1}(t + T/2)$. Circles highlight discernible vortex patterns that map to each other via R_y . Multimedia view: <https://doi.org/10.1063/5.0061658.2>

Pre-periodic flows have been observed in previous experimental studies^{20,21} of Q2D flows. However, their symmetry properties have received little attention. For instance, visual inspection of Fig. 1 in Danilov *et al.*²¹ reveals that the oscillatory flow that branches out of a 2×2 lattice of rectangular vortices is R_π -invariant. The R_x and R_y symmetries in the flow are broken via a Hopf bifurcation. Snapshots shown in Danilov *et al.*, which are separated in time by half an oscillation period, can be nearly mapped to each other via these broken symmetries despite experimental imperfections. In the present study, a similar symmetry-breaking scenario is observed in the $10 \times 9^-$ domain.

VI. SYMMETRY-BREAKING SECONDARY BIFURCATIONS

Table III shows that stable time-periodic solutions in the $10 \times 9^\pm$ and 10×10 domains are invariant under one of the symmetries of Eq. (1). To test whether fully asymmetric flows emerge via bifurcations of these solutions, we computed their linear stability. A detailed account of computing the Floquet (eigen) vectors of time-periodic solutions can be found in Refs. 30, 42, 43, and 46. Here, we summarize the key steps involved. To begin, we test whether an infinitesimal perturbation $d\mathbf{u}$ to \mathbf{u}_{po1} would grow or decay after one period T . In addition, we constrain $d\mathbf{u}$ to be orthogonal to $\hat{\mathbf{u}}_{po1}$ at $t = 0$, since a perturbation along $\hat{\mathbf{u}}_{po1}$ is equivalent to merely shifting the arbitrary origin of time on $\mathbf{u}_{po1}(t)$. The growth/decay of such perturbations (on a Poincaré section) transverse to $\hat{\mathbf{u}}_{po1}$ is then quantified using Floquet exponents^{39,46} λ'_k and vectors $\hat{\mathbf{e}}'_k$. The primes here distinguish these quantities from their steady flow counterparts [cf. Eq. (3)].

Let $\lambda'_1 = \sigma'_1 + i\omega'_1$ and $\hat{\mathbf{e}}'_1 = \mathbf{e}'_r + i\mathbf{e}'_c$ be the leading Floquet exponent and vector, respectively, of a time-periodic solution \mathbf{u}_{po1} . If we add an infinitesimal perturbation $\epsilon\mathbf{e}'_r$ to $\mathbf{u}_{po1}(0)$, the resulting flow after one period T is

$$\mathbf{u}(T) = \mathbf{u}_{po1}(0) + \epsilon e^{\sigma'_1 T} [\mathbf{e}'_r \cos(\omega'_1 T) - \mathbf{e}'_c \sin(\omega'_1 T)]. \tag{15}$$

When λ'_1 and $\hat{\mathbf{e}}'_1$ are real, we set $\omega'_1 = 0$ and $\mathbf{e}'_r = \hat{\mathbf{e}}'_1$ in the above equation. Equation (15) shows that \mathbf{u}_{po1} is linearly unstable (stable) if $\sigma'_1 > 0$ ($\sigma'_1 < 0$), since the magnitude of an infinitesimal perturbation increases (decays) by a factor $e^{N\sigma'_1 T}$ after N periods. For $N \rightarrow \infty$, however, the growth of any perturbation is bounded due to nonlinearity and dissipation, leading to the formation of new solutions.

Floquet vectors of a time-periodic flow invariant under a twofold symmetry R are either symmetric or antisymmetric with respect to R , as in the case of steady flows. Similarly, symmetries of the Floquet vectors that turn unstable in a bifurcation govern the symmetries of solutions that consequently emerge. Hence, using Eq. (15) and numerical integration, we identified that time-periodic flows in the $10 \times 9^\pm$ and 10×10 domains undergo symmetry-breaking bifurcations at Re_2 (cf. Table III). Since tracing the resulting stable/unstable branches (e.g., two-tori) is computational challenging, we classify these bifurcations by drawing analogies with the pitchfork and Hopf bifurcations of steady flows discussed in Sec. V.

A. Subcritical pitchfork bifurcation

The R_x -invariant pre-periodic orbit \mathbf{u}_{po1} in the $10 \times 9^+$ domain undergoes a subcritical pitchfork bifurcation at $Re_2 \approx 210.1$. Above

TABLE IV. Symmetry-breaking bifurcations in a chessboard-like lattice of square vortices. Symmetries broken via each bifurcation are indicated beneath dashed arrows. Solid arrows indicate that symmetry is either restored or not broken. Steady, time-periodic, and quasi-periodic solutions are labeled as \mathbf{u}_k , \mathbf{u}_{pok} , and \mathbf{u}_{qpk} , respectively. Numerical subscripts “ k ” label the solutions uniquely and superscripts \pm indicate pairs of symmetry-related solutions. PO and PPO labels in parenthesis distinguish periodic and pre-periodic flows.

$N_x \times N_y$	Symmetries									
9×9	R_y	\mathbf{u}_0	Supercritical Hopf ----- R_y	\mathbf{u}_{p01} (PPO)						
$10 \times 9^+$	R_x, R_y, R_π	\mathbf{u}_0	Supercritical Forward Pitchfork ----- R_x, R_π	\mathbf{u}_1^\pm	Supercritical Backward Pitchfork ----- R_x, R_π	\mathbf{u}_0	Supercritical Hopf ----- R_y, R_π	\mathbf{u}_{p01} (PPO)	Subcritical Pitchfork ----- R_x	\mathbf{u}_{p03}^\pm (PPO)
$10 \times 9^-$	R_x, R_y, R_π	\mathbf{u}_0	Supercritical Hopf ----- R_x, R_y	\mathbf{u}_{p01} (PPO)	Supercritical Neimark-Sacker ----- R_π	\mathbf{u}_{qp1}				
9×10	R_π	\mathbf{u}_0	Subcritical Pitchfork ----- R_π	\mathbf{u}_4^\pm						
10×10	R_x	\mathbf{u}_0	Supercritical Hopf ----- None	\mathbf{u}_{p01} (PO)	Subcritical Neimark-Sacker ----- R_x	\mathbf{u}_{p02} (PPO)				

this Reynolds number, \mathbf{u}_{p01} turns unstable to perturbations along an R_x -antisymmetric Floquet vector. We found that DNS of flow slightly above the bifurcation converges to either of the fully asymmetric solutions \mathbf{u}_{p03}^\pm , which lie far away from \mathbf{u}_{p01} . Similar to \mathbf{u}_{p01} , \mathbf{u}_{p03}^\pm are also pre-periodic with respect to $R \in \{R_y, R_\pi\}$, that is, $R\mathbf{u}_{p03}^\pm(t) = \mathbf{u}_{p03}^\pm(t + T/2)$. This quaternary bifurcation in the $10 \times 9^+$ domain can be qualitatively understood using Fig. 8, where \mathbf{u}_0 and \mathbf{u}_4^\pm can be interpreted as the time-independent counterparts of \mathbf{u}_{p01} and \mathbf{u}_{p03}^\pm , respectively. From this comparison, we can also infer that at least two unstable solutions \mathbf{u}_{p02}^\pm , analogous to \mathbf{u}_1^\pm in Fig. 8, must exist for $Re < Re_2$. Efforts to compute these branches are under way and the exact subcritical scenario will be reported in a subsequent publication.

B. Supercritical Neimark-Sacker bifurcation

The R_π -invariant pre-periodic orbit \mathbf{u}_{p01} in the $10 \times 9^-$ domain turns unstable via a supercritical Neimark-Sacker (or secondary Hopf) bifurcation at $Re_2 \approx 194.9$. The real part of the leading Floquet exponent $\sigma_1 \pm i\omega_1'$ of \mathbf{u}_{p01} , associated with an R_π -antisymmetric Floquet vector pair, changes sign at this Reynolds number. DNS of flow above the bifurcation converges to a quasi-periodic solution \mathbf{u}_{qp1} whose dynamics are characterized by two incommensurate frequencies: $\omega = 2\pi/T$ related to the period of \mathbf{u}_{p01} and ω_1' related to its unstable Floquet exponent [cf. Eq. (15)]. Supplementary material video 2 shows side-by-side evolution of \mathbf{u}_{qp1} and the plot of $\|\mathbf{u}_{qp1}\|$, to illustrate the presence of two incommensurate frequencies. Flow fields on \mathbf{u}_{qp1} never recur in time exactly and, as a result, \mathbf{u}_{qp1} maps to a closed curve on a Poincaré section transverse to \mathbf{u}_{p01} . Hence, this secondary bifurcation in the $10 \times 9^-$ domain is qualitatively similar to the supercritical Hopf bifurcation of a steady flow (cf. Fig. 10).

C. Subcritical Neimark-Sacker bifurcation

Table III shows that Hopf bifurcation of the primary solution in the 10×10 domain preserves the R_x -invariance of flow. The resulting time-periodic solution \mathbf{u}_{p01} , however, turns unstable at $Re_2 \approx 178.8$

via a symmetry-breaking Neimark-Sacker bifurcation. Slightly above the instability, DNS of flow converges to an asymmetric pre-periodic orbit \mathbf{u}_{p02} that is disconnected from \mathbf{u}_{p01} . Hence, the transition is subcritical in nature. An unstable two-torus that branches out of \mathbf{u}_{p01} must exist for $Re < Re_2$. Computing and continuing such solutions are computationally expensive and beyond the scope of the present study. Nevertheless, one may find some insightful discussion in this regard in Refs. 47 and 48.

Symmetry-breaking bifurcations of the square vortex flow in each domain we studied are summarized in Table IV. Except in the $10 \times 9^+$ domain, a fully asymmetric flow emerges immediately after the primary or secondary bifurcation. Even in the $10 \times 9^+$ domain, the forward and backward pitchfork bifurcations have mutually canceling symmetry-breaking effects. Hence, the square vortex flow in this domain becomes asymmetric effectively after two bifurcations: the supercritical Hopf and a subcritical pitchfork.

Table IV also reveals that different types of asymmetric solutions, at times with twofold multiplicity, are formed as a result of symmetry-breaking bifurcations. For instance, two symmetry-related steady and pre-periodic flows are formed in the 9×10 and $10 \times 9^+$ domains, respectively. In contrast, a single pre-periodic orbit is formed in the 9×9 and 10×10 domains, whereas a single quasi-periodic solution is observed in the $10 \times 9^-$ domain.

VII. SUMMARY AND CONCLUSIONS

In this article, we identified symmetry-breaking bifurcations in a laterally bounded two-dimensional flow composed of nearly square vortices. The flow satisfied no-slip velocity boundary conditions and was driven by forcing that is nearly sinusoidal in both spatial directions, closely mimicking shallow electrolyte layer experiments with a chessboard-like arrangement of magnets. As in an experiment, we chose an integer or half-integer number of forcing wavelengths along each direction and generated square vortex flows with different spatial symmetries. In addition to characterizing such symmetric flows at low Reynolds numbers, we also analyzed their spatial deformation and

linear stability with increasing Re . We then identified symmetry-breaking primary bifurcations and thoroughly analyzed the resulting secondary solutions. Finally, we traced the secondary (as well as tertiary, quaternary) bifurcations that lead to the formation of flows devoid of any spatial symmetry.

The key findings of this study are summarized below:

1. When a square (or rectangular) vortex flow on a laterally bounded domain is invariant under all symmetries of the governing equation (cf. Table II), it ceases to be invariant under reversing the direction of forcing. Even though previous experimental studies²¹ identified this sensitivity, we theoretically rationalized it using symmetry arguments and confirmed the sensitivity using DNS.
2. A chessboard-like lattice of square vortices driven by a nearly sinusoidal forcing undergoes gradual spatial deformation as Re increases.^{4,21} Specifically, we identified that a strictly sinusoidal approximation of the flow is accurate only up to $Re \approx 120$, which is well below the point of primary instability in the flow domains we studied.
3. The nature of primary bifurcation in a square vortex flow is sensitive to the symmetries of the governing equation and the direction of forcing. Striking examples of this were flows in the $10 \times 9^+$ and 9×10 domains, which have identical lateral extent and are governed by Eq. (1) with the same parameters (γ, β). Yet, three different types of primary bifurcations were identified: super/sub-critical pitchfork and supercritical Hopf. Previously, these three bifurcations were observed^{12,21} only across square/rectangular vortex flows with dissimilar lateral extent and frictional drag.
4. Even though the primary instability in a square vortex flow was studied^{5,8} earlier, secondary solutions that emerge via a bifurcation were not characterized using DNS. We computed both stable and unstable secondary solutions that branch out of the square vortex flow, analyzed their symmetries, and continued them in Re until they undergo a secondary instability. We also showed that “amplitudes” of secondary solutions, which are formed due to the nonlinear saturation of an instability, scale with Re as per theoretical predictions^{1–3} inside a narrow interval of Reynolds number near the bifurcation point.
5. Subcritical primary bifurcation in a square vortex flow was not explored previously in numerics, to the best of our knowledge. Combining the numerical integrator with a Newton solver and a branch continuation code, we mapped out a subcritical transition scenario that involves “snaking” of a solution branch (cf. Fig. 8). Even though this bifurcation is qualitatively similar to that reported in Sommeria,¹² the flow we studied did not transition to chaos directly. Such a transition, however, may occur for a different set of model parameters and domain size.
6. The breaking of spatial symmetries in a square vortex flow received limited attention in previous studies.¹¹ The present study is the first to explore this aspect comprehensively. We identified a gallery of symmetry-breaking pitchfork and Hopf bifurcations, both supercritical and subcritical in nature, of steady as well as time-periodic solutions (Table IV). We demonstrated that these bifurcations, in sequence, lead to a rich variety of fully asymmetric flows: symmetry-related pairs of steady or

time-periodic solutions, pre-periodic solutions, and quasi-periodic solutions.

Our results also highlight the need for further numerical and experimental exploration of transition to chaos/turbulence in the square vortex flow. Previously, Braun *et al.*¹⁰ have numerically identified a period-doubling route to chaos in a linear array of square vortices. The authors reported that the exact bifurcation sequence was, however, sensitive to the choice of no/free-slip boundary conditions. In experiments, Michel *et al.*¹¹ observed an intermittency route to chaos in a 2×4 lattice of vortices. Variability in the multiplicity of fully asymmetric solutions in Table IV suggests that different routes to chaos may be observed in the square vortex flows analyzed in this study. We intend to explore this question and report the findings in a subsequent publication.

Recent theoretical^{13,49} and experimental¹¹ studies of steadily forced 2D flows have also identified the coexistence of distinct “asymmetric” turbulent states and flow transitions between them. Whether symmetries of the forcing profile influence the formation and dynamics of such states is currently open for exploration. Finally, whether a laboratory realization (described in the supplementary material) of the 2D flow we analyzed here will undergo the same sequence of bifurcations (as its 2D DNS) needs to be explored.^{25,50} If it indeed does, the square vortex flow should serve as an ideal platform to demonstrate hydrodynamic stability in a pedagogical setting,⁵¹ given the ease of its experimental and numerical realizations.

SUPPLEMENTARY MATERIAL

See the supplementary material for Text: (1) Description of experimental setup theoretically modeled in this study and (2) analytical estimates for 2D model parameters, including Reynolds number, from experimental parameters. **Videos:** (1) R_x -invariant time-periodic flow in the 10×10 domain and (2) asymmetric quasi-periodic flow in the $10 \times 9^-$ domain.

APPENDIX A: THE NEWTON METHOD

Unlike a linearly stable solution to Eq. (1), unstable steady flows cannot be computed using mere numerical integration. To compute such solutions, we employed the Newton method, which iteratively solves the nonlinear equation $\mathbf{F}(\mathbf{u}_{eq}) = 0$ starting from an initial guess \mathbf{u}_{ic} that satisfies the criterion $\mathbf{F}(\mathbf{u}_{ic}) \approx 0$. A detailed discussion of the solver is beyond the scope of this study. Nevertheless, we provide a brief overview of the Newton method in the following. Given the initial guess \mathbf{u}_{ic} , the goal is to identify $d\mathbf{u}$ such that $\mathbf{F}(\mathbf{u}_{ic} + d\mathbf{u}) = 0$. Since a direct solution to this nonlinear equation is not computationally feasible, we seek an approximate solution, as a first step, using the linear equation

$$\mathbf{F}(\mathbf{u}_{ic}) + \mathbf{J}(\mathbf{u}_{ic})d\mathbf{u} = 0, \quad (\text{A1})$$

where \mathbf{J} is the Jacobian matrix (cf. Sec. II B). Since the dimensions of \mathbf{J} are very large ($\approx 10^5 \times 10^5$), the above equation is solved for $d\mathbf{u}$ using the generalized minimal residual method (GMRES), which is a Krylov subspace method.⁵² Note that $d\mathbf{u}$ so obtained does not satisfy $\mathbf{F}(\mathbf{u}_{ic} + d\mathbf{u}) = 0$; hence, we update $\mathbf{u}_{ic} \rightarrow \mathbf{u}_{ic} + d\mathbf{u}$ after each Newton iteration. For a sufficiently “good” initial guess \mathbf{u}_{ic} , the

solver converges to an unstable solution $\mathbf{u}_{eq} = \mathbf{u}_{ic} + d\mathbf{u}$ in only a few iterations. More details regarding Newton–Krylov solvers can be found in Refs. 30, 42, and 53–55.

APPENDIX B: PARABOLIC BRANCH CONTINUATION TECHNIQUE

Equation (1) can possess multiple stable/unstable equilibrium solutions \mathbf{u}_{eq} at the same Re , as illustrated in Fig. 8. Hence, both DNS and the Newton solver can converge to a solution that is far away from the desired one, if initialized with a poorly constructed initial guess \mathbf{u}_{ic} . Convergence to the desired \mathbf{u}_{eq} can be tested by computing⁵⁶

$$\Delta_{ic} = \|\mathbf{u}_{ic} - \mathbf{u}_{eq}\| / \|\mathbf{u}_{eq}\|. \quad (B1)$$

Ideally, we should construct \mathbf{u}_{ic} such that $\Delta_{ic} \approx 0$. Near a bifurcation, separation between distinct solutions is often very small and this poses a challenge, since $\Delta_{ic} \approx 0$ for convergence to any solution. To overcome this problem, we employed the following three-point parabolic branch continuation technique to extrapolate solutions in Re .

Let \mathbf{u}_k for $k \in \{0, 1, 2\}$ represent steady solutions on a branch at three closely spaced Reynolds numbers Re_k , that is, $|Re_{k+1}/Re_k - 1| \ll 1$. When initializing branch continuation, it is preferable to choose Re_k slightly away from a bifurcation point. We then define a parabola

$$\mathbf{p}(Re) = \mathbf{c}_0 + \mathbf{c}_1 Re + \mathbf{c}_2 Re^2, \quad (B2)$$

where the relations $\mathbf{p}(Re_k) = \mathbf{u}_k$ determine the coefficients $(\mathbf{c}_0, \mathbf{c}_1, \mathbf{c}_2)$. To construct the initial guess for a solution on this branch, for instance at $Re = Re_2 + dRe$, we simply evaluate $\mathbf{p}(Re_2 + dRe)$. The solution \mathbf{u}_{eq} at this Reynolds number is then computed using DNS and the Newton solver. The step size dRe is iteratively chosen such that Δ_{ic} is less than a set upper limit.

APPENDIX C: PRE-PERIODIC ORBITS

In Sec. VC, we visualized the oscillations of \mathbf{u}_{p01} using orthogonal coordinates p_1 and p_2 . Instead, one can also project \mathbf{u}_{p01} directly onto the real and imaginary parts of $\hat{\mathbf{e}}_1^\pm = \mathbf{e}_r \pm i\mathbf{e}_c$, the unstable eigenvector pair of the primary solution \mathbf{u}_0

$$\mathbf{u}_{p01}(t) = \mathbf{u}_0 + C[\mathbf{e}_r \cos(\omega t) - \mathbf{e}_c \sin(\omega t)]. \quad (C1)$$

If $\hat{\mathbf{e}}_1^\pm$ is R -antisymmetric, that is, $Re_r = -\mathbf{e}_r$ and $Re_c = -\mathbf{e}_c$, it is straightforward to show using the above equation that

$$R\mathbf{u}_{p01}(t) = \mathbf{u}_0 - C[\mathbf{e}_r \cos(\omega t) - \mathbf{e}_c \sin(\omega t)]. \quad (C2)$$

By substituting $\cos(\omega t) = -\cos(\omega t + \pi)$, $\sin(\omega t) = -\sin(\omega t + \pi)$, and $\omega T/2 = \pi$, we arrive at the relation $R\mathbf{u}_{p01}(t) = \mathbf{u}_{p01}(t + T/2)$ that defines a pre-periodic orbit.

Equation (C1) describes oscillations of $\mathbf{u}_{p01}(t)$ in a skew coordinate system, when \mathbf{e}_r and \mathbf{e}_c are not mutually orthonormal vectors. In this coordinate system, the phase portraits of \mathbf{u}_{p01} are circles of radius C , which are traversed at uniform angular speed ω close to the bifurcation point. The elliptical shape of the orbits in

Fig. 10(a) and variations in the instantaneous speed $\sqrt{\dot{p}_1^2 + \dot{p}_2^2}$ are consequences of non-normality of \mathbf{e}_r and \mathbf{e}_c . Nevertheless, Eq. (12) can be derived from Eq. (C1) by performing Gram–Schmidt orthonormalization of \mathbf{e}_r and \mathbf{e}_c .

DATA AVAILABILITY

The data that support the findings of this study are available from the author upon reasonable request. MATLAB code to perform DNS of the 2D model is available here (<https://github.com/balachandrasuri/2DModelDNS.git>).

REFERENCES

- ¹J. D. Crawford, “Introduction to bifurcation theory,” *Rev. Mod. Phys.* **63**, 991–1037 (1991).
- ²J. D. Crawford and E. Knobloch, “Symmetry and symmetry-breaking bifurcations in fluid dynamics,” *Annu. Rev. Fluid Mech.* **23**, 341–387 (1991).
- ³R. Seydel, *Practical Bifurcation and Stability Analysis* (Springer Science and Business Media, 2009), Vol. 5.
- ⁴J. Verron and J. Sommeria, “Numerical simulation of a two-dimensional turbulence experiment in magnetohydrodynamics,” *Phys. Fluids* **30**, 732–739 (1987).
- ⁵A. Thess, “Instabilities in two-dimensional spatially periodic flows. II. Square eddy lattice,” *Phys. Fluids A* **4**, 1396–1407 (1992).
- ⁶J. Tithof, B. C. Martell, and D. H. Kelley, “Three-dimensionality of one- and two-layer electromagnetically driven thin-layer flows,” *Phys. Rev. Fluids* **3**, 064602 (2018).
- ⁷A. Alexakis, “Three-dimensional instabilities and negative eddy viscosity in thin-layer flows,” *Phys. Rev. Fluids* **3**, 114601 (2018).
- ⁸Z.-M. Chen, “Instability of two-dimensional square eddy flows,” *Phys. Fluids* **31**, 044107 (2019).
- ⁹Z.-M. Chen, “Bifurcating steady-state flows involving energy dissipation over Hartmann boundary layer,” [arXiv:2105.00742](https://arxiv.org/abs/2105.00742) (2021).
- ¹⁰R. Braun, F. Feudel, and P. Guzdar, “Route to chaos for a two-dimensional externally driven flow,” *Phys. Rev. E* **58**, 1927 (1998).
- ¹¹G. Michel, J. Hérault, F. Pétrélis, and S. Fauve, “Bifurcations of a large-scale circulation in a quasi-bidimensional turbulent flow,” *Europhys. Lett.* **115**, 64004 (2016).
- ¹²J. Sommeria, “Experimental study of the two-dimensional inverse energy cascade in a square box,” *J. Fluid Mech.* **170**, 139–168 (1986).
- ¹³P. K. Mishra, J. Hérault, S. Fauve, and M. K. Verma, “Dynamics of reversals and condensates in two-dimensional Kolmogorov flows,” *Phys. Rev. E* **91**, 053005 (2015).
- ¹⁴H. Xia and N. Francois, “Two-dimensional turbulence in three-dimensional flows,” *Phys. Fluids* **29**, 111107 (2017).
- ¹⁵A. van Kan and A. Alexakis, “Condensates in thin-layer turbulence,” *J. Fluid Mech.* **864**, 490–518 (2019).
- ¹⁶R. Ran, Q. Brosseau, B. C. Blackwell, B. Qin, R. Winter, and P. E. Arratia, “Bacteria hinder large-scale transport and enhance small-scale mixing in time-periodic flows,” [arXiv:2108.01049](https://arxiv.org/abs/2108.01049) [physics.flu-dyn] (2021).
- ¹⁷E. Beauvier, S. Bodea, and A. Pocheau, “Front propagation in a regular vortex lattice: Dependence on the vortex structure,” *Phys. Rev. E* **96**, 053109 (2017).
- ¹⁸T. D. Nevins and D. H. Kelley, “Front tracking velocimetry in advection-reaction-diffusion systems,” *Chaos: Interdiscip. J. Nonlinear Sci.* **28**, 043122 (2018).
- ¹⁹N. T. Baker, A. Pothérat, L. Davoust, F. Debray, and R. Klein, “Controlling the dimensionality of low-Rm MHD turbulence experimentally,” *Exp. Fluids* **58**, 1–14 (2017).
- ²⁰A. Batchaev, “Self-oscillations in an elementary cell of a doubly periodic quasi-two-dimensional flow,” *Izv. Atmos. Oceanic Phys.* **39**, 401–412 (2003).
- ²¹S. D. Danilov, F. V. Dolzhanskii, V. A. Dovzhenko, and V. A. Krymov, “An advanced investigation of interaction of allocated quasi two dimensional vortices,” *Chaos: Interdiscip. J. Nonlinear Sci.* **6**, 297–308 (1996).
- ²²K. Gotoh and M. Yamada, “Instability of a cellular flow,” *J. Phys. Soc. Jpn.* **53**, 3395–3398 (1984).

- ²³H. Fukuta and Y. Murakami, “Effect of lateral boundaries on large-scale mode: Linear stability of square cell flows in rectangular regions,” *J. Phys. Soc. Jpn.* **65**, 1655–1665 (1996).
- ²⁴H. Fukuta and Y. Murakami, “Vortex merging, oscillation, and quasiperiodic structure in a linear array of elongated vortices,” *Phys. Rev. E* **57**, 449–459 (1998).
- ²⁵J. Tithof, B. Suri, R. K. Pallantla, R. O. Grigoriev, and M. F. Schatz, “Bifurcations in a quasi-two-dimensional Kolmogorov-like flow,” *J. Fluid Mech.* **828**, 837–866 (2017).
- ²⁶B. Suri, J. Tithof, R. Mitchell, R. O. Grigoriev, and M. F. Schatz, “Velocity profile in a two-layer Kolmogorov-like flow,” *Phys. Fluids* **26**, 053601 (2014).
- ²⁷S. Armfield and R. Street, “The fractional-step method for the Navier–Stokes equations on staggered grids: The accuracy of three variations,” *J. Comput. Phys.* **153**, 660–665 (1999).
- ²⁸The parameter $\gamma = (\pi w/2h)^2$ is related to the ratio of the horizontal (forcing) length scale w and the fluid layer thickness h in laboratory experiments.
- ²⁹Y. Saad, *Numerical Methods for Large Eigenvalue Problems*, revised ed. (SIAM, 2011).
- ³⁰G. J. Chandler and R. R. Kerswell, “Invariant recurrent solutions embedded in a turbulent two-dimensional Kolmogorov flow,” *J. Fluid Mech.* **722**, 554–595 (2013).
- ³¹J. F. Gibson, J. Halcrow, and P. Cvitanović, “Visualizing the geometry of state space in plane Couette flow,” *J. Fluid Mech.* **611**, 107–130 (2008).
- ³²F. V. Dolzhanskii, V. A. Krymov, and D. Y. Manin, “Stability and vortex structures of quasi-two-dimensional shear flows,” *Sov. Phys. Usp.* **33**, 495–520 (1990).
- ³³B. Suri, L. Kageorge, R. O. Grigoriev, and M. F. Schatz, “Capturing turbulent dynamics and statistics in experiments with unstable periodic orbits,” *Phys. Rev. Lett.* **125**, 064501 (2020).
- ³⁴D. Lucas and R. R. Kerswell, “Spatiotemporal dynamics in two-dimensional Kolmogorov flow over large domains,” *J. Fluid Mech.* **750**, 518–554 (2014).
- ³⁵F. Romanò, “Stability of generalized Kolmogorov flow in a channel,” *Phys. Fluids* **33**, 024106 (2021).
- ³⁶It is straightforward to validate the linear response using the vorticity equation, which is obtained by taking the curl of Eq. (1). The nonlinear term $\mathbf{u} \cdot \nabla \omega$ for low- Re flows is nearly zero and increases with increasing Re .
- ³⁷The signs \pm assigned to an eigenvector are arbitrary.
- ³⁸The forward and backward pitchfork bifurcations can be quantitatively characterized using the same procedure when the control parameter Re is varied in opposite directions. Specifically, we found that Eq. (8) accurately approximates the branches \mathbf{u}_1^\pm close to Re_{p2} and the Reynolds number dependence of the amplitude ε obeys a square root scaling $\varepsilon \propto \sqrt{Re_{p2} - Re}$.
- ³⁹S. H. Strogatz, *Nonlinear Dynamics and Chaos: With Applications to Physics, Biology, Chemistry, and Engineering* (Westview Press, 2014).
- ⁴⁰We tested that solution branches approach each other along the marginal eigenvector near a saddle-node bifurcation. Also, the separation between the solutions follows a square root scaling with Re .
- ⁴¹D. Ruelle and F. Takens, “On the nature of turbulence,” *Commun. Math. Phys.* **20**, 167–192 (1971).
- ⁴²D. Viswanath, “Recurrent motions within plane Couette turbulence,” *J. Fluid Mech.* **580**, 339–358 (2007).
- ⁴³S. Altmeyer, Y. Do, F. Marques, and J. M. Lopez, “Symmetry-breaking Hopf bifurcations to 1-, 2-, and 3-tori in small-aspect-ratio counterrotating Taylor–Couette flow,” *Phys. Rev. E* **86**, 046316 (2012).
- ⁴⁴G. Arioli and H. Koch, “A Hopf bifurcation in the planar Navier–Stokes equations,” *J. Math. Fluid Mech.* **23**, 70 (2021).
- ⁴⁵P. Cvitanović and J. F. Gibson, “Geometry of the turbulence in wall-bounded shear flows: Periodic orbits,” *Phys. Scr.* **2010**, 014007.
- ⁴⁶P. Cvitanović, R. Artuso, R. Mainieri, G. Tanner, and G. Vattay, *Chaos: Classical and Quantum* (Niels Bohr Institute, Copenhagen, 2012).
- ⁴⁷T. Itano and S. Toh, “The dynamics of bursting process in wall turbulence,” *J. Phys. Soc. Jpn.* **70**, 703–716 (2001).
- ⁴⁸B. Suri, R. K. Pallantla, M. F. Schatz, and R. O. Grigoriev, “Heteroclinic and homoclinic connections in a Kolmogorov-like flow,” *Phys. Rev. E* **100**, 013112 (2019).
- ⁴⁹Y. Hiruta and S. Toh, “Intermittent direction reversals of moving spatially localized turbulence observed in two-dimensional Kolmogorov flow,” *Phys. Rev. E* **96**, 063112 (2017).
- ⁵⁰P. A. Reinbold, L. M. Kageorge, M. F. Schatz, and R. O. Grigoriev, “Robust learning from noisy, incomplete, high-dimensional experimental data via physically constrained symbolic regression,” *Nat. Commun.* **12**, 3219 (2021).
- ⁵¹D. H. Kelley and N. T. Ouellette, “Using particle tracking to measure flow instabilities in an undergraduate laboratory experiment,” *Am. J. Phys.* **79**, 267–273 (2011).
- ⁵²Y. Saad and M. H. Schultz, “GMRES: A generalized minimal residual algorithm for solving nonsymmetric linear systems,” *SIAM J. Sci. Stat. Comput.* **7**, 856–869 (1986).
- ⁵³C. Kelley, *Iterative Methods for Linear and Nonlinear Equations* (Society for Industrial and Applied Mathematics, 1995).
- ⁵⁴C. Kelley, *Solving Nonlinear Equations with Newton’s Method* (SIAM, 2003).
- ⁵⁵R. Mitchell, “Transition to turbulence and mixing in a quasi-two-dimensional Lorentz force-driven Kolmogorov flow,” Ph.D. thesis (Georgia Institute of Technology, 2013).
- ⁵⁶B. Suri, J. Tithof, R. O. Grigoriev, and M. F. Schatz, “Unstable equilibria and invariant manifolds in quasi-two-dimensional Kolmogorov-like flow,” *Phys. Rev. E* **98**, 023105 (2018).